2023-08-01

Partial Auto-correlation of Low Magnitude Earthquakes from the 2016 IRIS Aray in Grant County, Oklahoma

Alex Christopher Eddy
University of Texas at El Paso

Recommended Citation

Eddy, Alex Christopher, "Partial Auto-correlation of Low Magnitude Earthquakes from the 2016 IRIS Aray in Grant County, Oklahoma" (2023). *Open Access Theses & Dissertations*. 3908.
https://scholarworks.utep.edu/open_etd/3908

PARTIAL AUTO-CORRELATION OF LOW MAGNITUDE EARTHQUAKES FROM THE 2016 IRIS ARRAY IN GRANT COUNTY, OKLAHOMA

ALEX CHRISTOPHER EDDY

Master's Program in Geophysics

APPROVED:

Steven Harder, Ph.D., Chair

Marianne Karplus, Ph.D.

Harold Gurrola, Ph.D.

Stephen L. Crites, Ph.D.
Dean of the Graduate School

PARTIAL AUTO-CORRELATION OF LOW MAGNITUDE EARTHQUAKES FROM THE 2016 IRIS ARRAY IN GRANT COUNTY, OKLAHOMA

by

ALEX CHRISTOPHER EDDY, B.S.

THESIS

Presented to the Faculty of the Graduate School of
The University of Texas at El Paso
in Partial Fulfillment
of the Requirements
for the Degree of

MASTER OF SCIENCE

Department of Earth, Environmental, and Resource Sciences

THE UNIVERSITY OF TEXAS AT EL PASO

August 2023

ABSTRACT

The Anadarko Basin in is a seismically active basin that spans central and western Oklahoma into Kansas. In June and July of 2016, the IRIS Community Wavefield Experiment array was deployed for approximately a month, recording over 300 earthquakes. Using 4 of these earthquakes and an east – west array of 129 Fairfield Nodal Z-land 3C nodes, I present a novel application of correlation. These four earthquakes with a M_L of 2.8-3.0 represent a varied azimuthal distribution and are between 9 and 40km from the array and have a frequency peak at approximately 10 Hz.

As a proof of concept, the presented method of partial auto-correlation uses the first arrival from the entire array to correlate the array traces rather that a single trace (cross correlation) or the trace itself (autocorrelation). The results show a reduction in seismic noise as expected from a correlation, as well as strengthened horizons and feature clarifications such as fractures. Isopach maps and a nearby well log were used to define a stratigraphic column for geologic interpretation. The core theory of this method is built on taking advantage of multiples and the results show improvements of multiples after the first. The results presented show promise for further application of this method that can lead to a process of generating pseudo 3D models using new midpoints after virtually transferring the source to a multiple's reflection point on the surface. To do this, the virtual source midpoint will need to identified and the method will need to be designed to handle non-linear arrivals.

TABLE OF CONTENTS

LIST OF TABLES

LIST OF FIGURES

INTRODUCTION

In 2016 the Oklahoma Geological Survey (OGS) reported 4,253 earthquakes within the state. 3,627 of these earthquakes had a magnitude (M) of 3 or lower, 626 with a M 3 to 5, and only three being M ≥ 5 (OGS, 2017). Most of these earthquakes occurred in central Oklahoma around Oklahoma City and to the north and west forming an arc convex to the northeast. Figure 1 shows a subset of earthquakes but is also representative of most 2016 events. Event outliers are located closer to the deep Anadarko basin, on the Cherokee platform, or associated with one of the southern fault complexes (Chopra et al., 2018). When combined with the local geology and abundance of low magnitude sources, this area provides a testing ground for novel methods of seismic processing that take advantage of low magnitude sources, which is the purpose of this thesis.

This project uses data recorded from June 21, 2016 to July 20, 2016, when the Incorporated Research Institutions for Seismology (IRIS) Community Wavefield Experiment, referred to as the YW array (Anderson et al., 2016) was deployed on the Anadarko basin shelf. During this time 348 earthquakes were recorded (Fig. 1) ranging in magnitude from 1.0 to 4.4. The study area is located north-central Oklahoma in Grant County. Although the YW array had several sensor configurations, only the 129 east-west sensors, numbered 1001 to 1129, will be used (Figure 2). Also shown in Fig. 2, is a generalization of the western fault lines of the Nemaha Uplift to show proximity to the significant seismic zone. This was illustrated using the Oklahoma fault map (Marsh and Holland, 2016) and basement elevation (Crain and Chang, 2018).

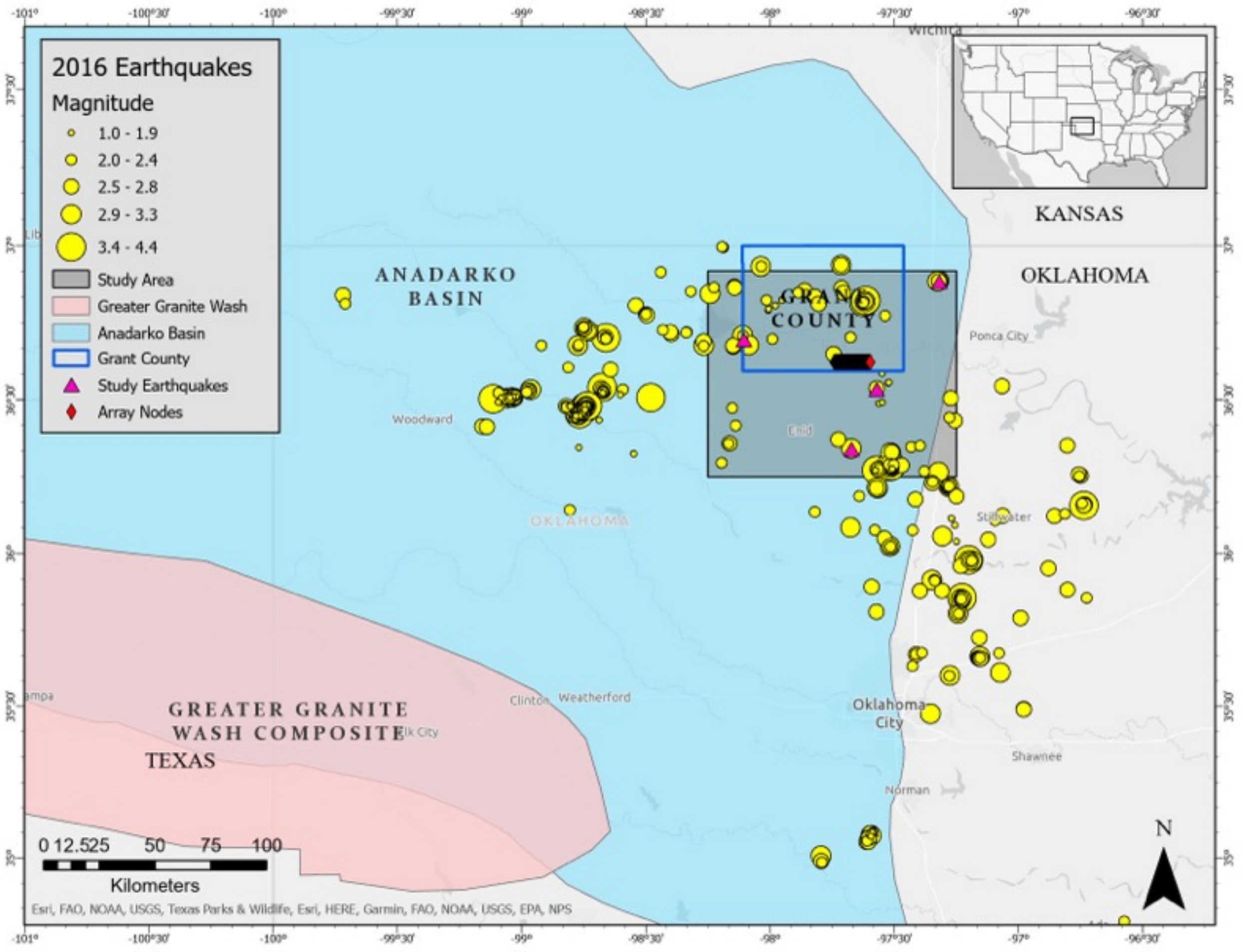

Figure 1: Map of the 348 magnitude scaled earthquakes (yellow circles) registered by the OGS in Oklahoma from June 21 to July 20, 2016. The dark grey rectangle shows the study area in Figure 2. The Anadarko basin province is shown as a translucent blue polygon, and the Greater Granite Wash Composite in red for spatial reference (USGS, 2011). Earthquake data from the OGS (2017). Grant County is outlined in blue and labeled. The array nodes are red diamonds in southern Grant County with node 1001 to the west and 1129 to the east. Pink triangles (not magnitude scaled) within the Grant County box show the location of the study earthquakes, detailed in Figure 2.

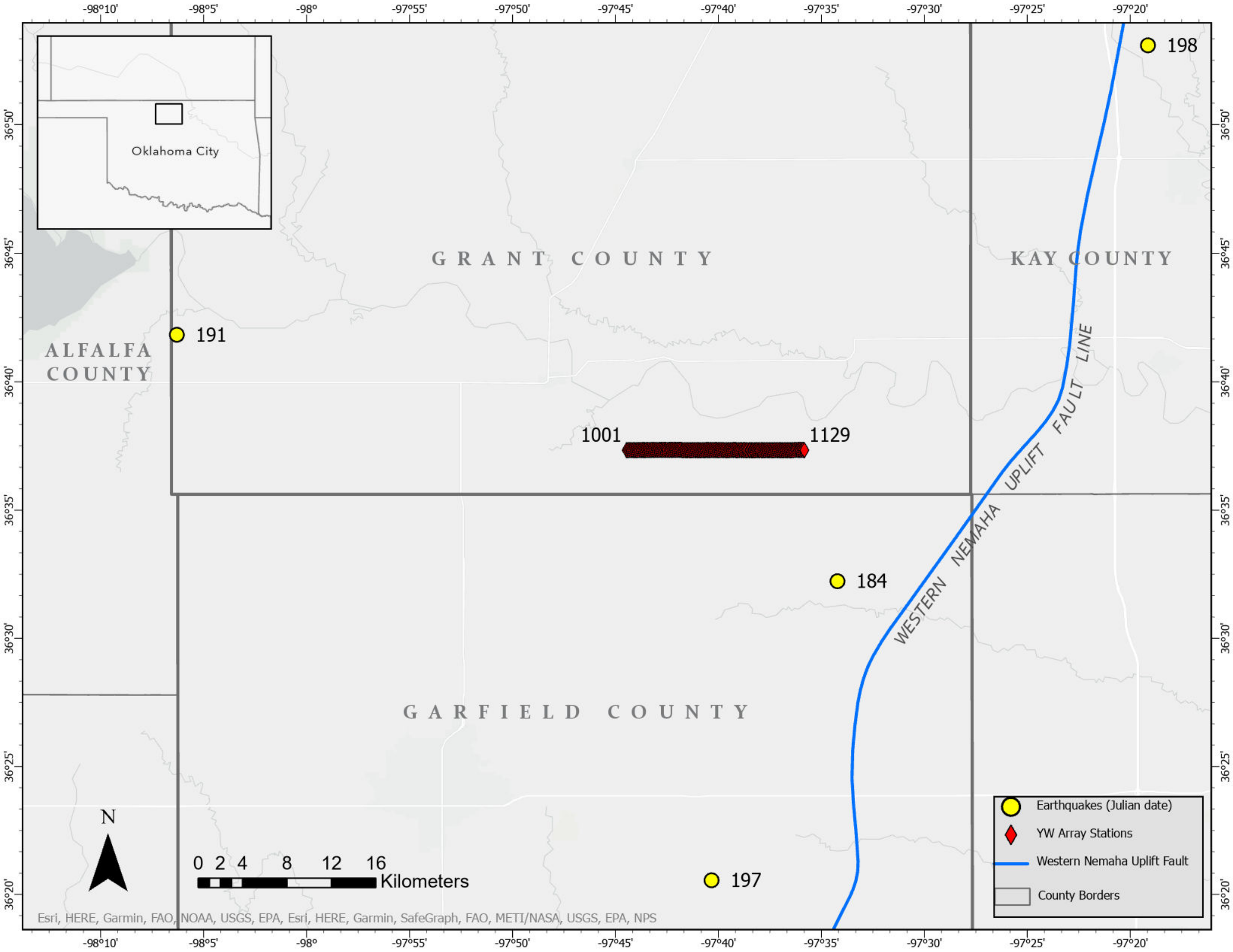

Figure 2: Map of the dark grey area shown in Figure 2 of the east-west nodes of the array and selected earthquakes used for this study. The 129 seismometers in this line are Fairfield Z-Land 3-component nodes (red diamonds), 1001 being the first node to the west and 1129 being the last on the east of the array. The node location data was acquired from the IRIS DMC (IRIS, 2017). Yellow circles show the locations of earthquakes used in this study. A simplified Nemaha Uplift fault line has been illustrated in blue.

Because of the nature and azimuthal distribution of earthquakes relative to the array, a form of interferometry will be used on selected events. There are four selected events (Fig. 2) that are meant to simulate a small active source at varying azimuths and distances from the array and should contain enough high frequency data to see individual layers of the basin shelf. Application of this correlation method will demonstrate a visual improvement to the seismic resolution. Further application of this method derived from Torii et al. (2007) can transform a single source into a number of virtual sources equal to the number of seismometers minus one, creating midpoints between each virtual source and receiver. When applied to a distribution of earthquakes around the receivers, these midpoints could be used to construct a 3D image from fewer recording devices and fewer sources than traditionally needed for a 3D volume. This will be covered in more detail in the theory section. Applying this in a practical scenario would require careful planning for source size and distribution to ensure a useful frequency content and azimuthal coverage, and return an improved efficiency of useable data for a smaller amount of equipment and man hours on a deployment. Applicable scenarios include surveys with limited budgets and difficult to reach areas where equipment may be a limiting factor.

ORIGINS OF INTERFEROMETRY IN SEISMOLOGY

Seismic interferometry originates from the reflection and transmission problems in a multilayered model (Claerbout, 1968). Haskell (1953) provided the first computationally satisfactory treatment of surface wave dispersion in a multilayered media. Sherwood and Trorey (1965) expanded on Haskell's matrix method to define the transmission of compressional waves travelling upwards and downwards through a multilayered model. Claerbout (1968) applied a finite energy value to the transmitted wave in the Sherwood and Trorey (1965) equation, which resulted in a formal statement of the results by Kuntez and d'Erceville (1962) whom first addressed the reflection problem. The inversion problem for solving the medium will be stable if the observed reflection seismogram is one side of an autocorrelation. Claerbout (1965) applied the simplified Haskell-Sherwood and Trorey transmission equation to the formalized Kuntez reflection equation. The result states that the reflection seismogram from a surface source and a surface receiver is one side of the autocorrelation of the seismogram from a source at depth and the same receiver. Claerbout's 1D conjecture was later proven for a lossless 3D inhomogeneous medium (Wapenaar et al., 2002, 2004) and was applied by Draganov (2006) to reconstruct the reflection response for deterministic and diffuse fields. Interferometry has successfully been applied to studies using varied data types that range from 100 micro-earthquakes (Torii et al., 2007) to ambient noise studies utilizing several hours of data (Draganov et al., 2013) to month long recordings (Krzywosz, 2015), and is a viable method for longer record processing.

THEORY AND PREVIOUS STUDIES

Interferometry originated from Christiaan Huygen in 1678 when he proposed that each point that light reaches acts as a new source that radiates light spherically from each point. In 1818 Augustin-Jean Fresnel further refined Huygen's principle in his publication of "Memoir on the Diffraction of Light" where he provided a quantitative description of light diffraction and interference. This established the Huygen-Fresnel principle. Many effects of this principle can be demonstrated by shining light though a medium such as water or a prism, or the double-slit experiment. The study of how light waves constructively and destructively interact with each other became known as interferometry (Robinson et al., 2006) and can also be applied to any energy in the form of a wave including sound and seismic waves.

Consider a scenario with two sound waves of the same frequency and any amplitude (A_n) that originate near each other and travel in the same direction. When the two waves are synchronized (in phase; when the peaks align), the wave is amplified when they interact with each other. The characteristics of the wave at the point of interference are an unaltered frequency and an amplitude of $| A_{1max} + A_{2max} |$. In the opposite scenario when the two waves are perfectly asynchronous and one wave's peak aligns with the other wave's trough, the resulting amplitude at the point of interference is $| A_{1max} - A_{2max} |$. In this case when both amplitudes are the same, the resulting wave form will have zero amplitude for the duration of the interference zone, effectively cancelling the sound all together. For all cases where the two sound waves are not completely synchronized or asynchronous, the amplitude will be between zero and $| A_{1max} + A_{2max} |$.

Seismic interferometry applies the same constructive and destructive properties of interacting sound or light waves to seismic waves. Where seismic waves interfere constructively, this affirms a feature (subsurface layer) from both traces with a stronger response or larger signal amplitude. Deconstructive interference serves to eliminate non-coexisting features from both traces; if one record shows a layer and the other does not, the combination of these two segments will reduce the product's amplitude. Unlike a controlled sound test environment, seismic waves rarely originated from a specified location at perfect times. Because the subsurface rarely undergoes significant changes in structure, it can be assumed that data recordings from different times and locations (within reason) are recording the same structures. To extract the similarities between seismic records, a correlation can be performed. Cross correlations are used on records from different locations and autocorrelations are used a record at different times. The use of correlations was first suggested by Jon Claerbout (1968). He showed that the autocorrelation of a recording from an earthquake produces the seismic record as a vertically traveling seismic wave to the same recording station. This became the core of seismic interferometry.

Typically, seismic interferometry is performed on large data sets with either no distinct features or highly convoluted features. Respectively, these are seismic records from ambient seismic noise and teleseismic events. Both data sets often require several correlation iterations from multiple records or over a long period of time to fully extract subsurface features. Unlike these traditional applications of interferometry, this study uses local earthquake interferometry which applies interferometric methods to earthquakes recorded within 40km. At the local scale only a few seconds of P-wave data from the vertical record are required. The purpose of this method is to improve the seismogram quality by using significantly smaller data sets and lower magnitude sources rather than using larger sources or more data.

The second component of this study is to establish the functionality on which virtual source relocation can be applied. Source relocation is a principle that allows the data to be processed under the assumption that the seismic waves originated from another location along the ray path between the original hypocenter and the receiver. Based on Claerbout's (1968) description of how autocorrelated records of earthquakes at a distance are equivalent to a vertical recording, Wapenaar (2003) was able to show that of two receivers recording the same sources, one could be assigned the role of the source. This allows for a simplified reflection image between the two seismometers. Source relocation is not exclusive to the subsurface. Bakulin and Calvert (2006) presented a borehole reservoir monitoring solution by relocating sources from the surface to below the complex overburden, greatly simplifying the seismic processing and interpretation.

Using these established methods, Torii et al. (2007) demonstrated that earthquakes from at depth can be relocated to the surface near the array. Figure 3 shows a simplified concept of this method where nodes A and B initially receive a transmitted response (T) from the source. After performing interferometry on the data, node A receives a response (R) from B, the relocated source, that reflects off a midpoint between the two locations. This combines the concepts proposed by both Claerbout (1968) and Wapenaar (2003) and sets up a reflection image from a midpoint slightly offset from the array. When applied to earthquakes from various azimuths, the resulting offset seismic profiles can be assembled into a pseudo 3D volume. In the context of local earthquake interferometry, location B is where the seismic wave reflects off the surface and travels towards A by reflecting off the strata between A and B.

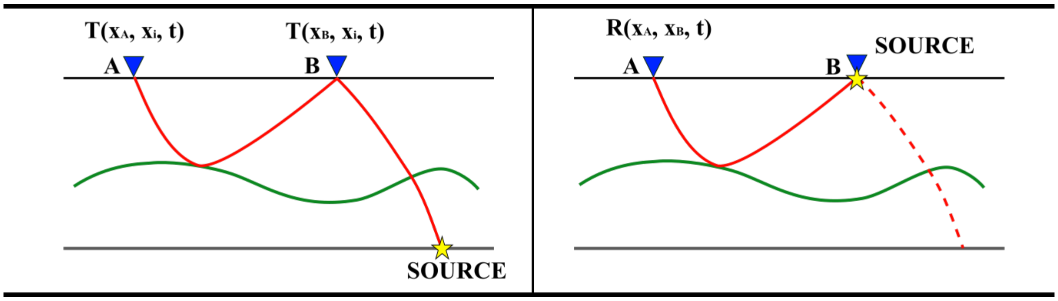

Figure 3: Modified illustration from Torii et al. (2007) showing the simplified concept of using interferometry to virtually transfer the source from the subsurface (left) to a surface virtual source (right). T indicates a transmitted response from the earthquake (located at x_i) at node A and B at time t. R indicated the reflected response at A from B. The seismogram at A after interferometry can be a reflected image from the midpoint between A and B.

APPLICATION OF CORRELATION FOR THIS STUDY

Autocorrelation is a specific case of correlation where a signal is correlated with itself and is commonly used to identify repetitious data sequences and patterns (Telford et. al, 1990). Conceptually, autocorrelation works by copying the targeted signal and sliding it across itself. This operation can be performed moving the copied signal either forward or reverse in time to generate positive and negative lags, respectively. Where the signal's wave form overlaps with little difference, a strong response is recorded in the correlogram (auto correlation function). Opposing and mismatched wave forms return a weak response or low amplitude on the correlogram.

Repeated signals return a stronger response in the correlogram while the response from noise will be reduced. In seismology, repetitious signals come from either repeated stratigraphy or from multiples where a seismic wave reverberates between layers and returns the same waveform later after the initial reflection has been recorded. However, because multiples are recorded later than they should be, according to the geologic profile, they are convolved with other recorded returning waves. Multiples are often not visually noticeable without other processing (e.g. frequency filtering), which may be necessary before autocorrelating the data for the targeted depth based on frequency content.

Mathematically, a correlation is a data set calculated as the summation of the product between corresponding samples from two data sets (x_t and y_t) traces, where the second trace shifts in the positive or negative direction relative to the first after each iteration, called a lag. In the case of an autocorrelation, both traces are the same (x_t *and* x_t). This calculation returns a single value per iteration which can be graphed over time as a correlogram.

Consider the following formula to calculate a correlation between two signals (φ_{xy}) as a function of displacement in number of samples or time (τ) and the sample number from the initial position (k).

$$\phi_{xy}(\tau) = \sum_k x_k y_{k+\tau}$$

For the first iteration at τ=0, trace x_k and y_k are the most similar or identical in the case of an autocorrelation where a signal is placed on top of itself, and each product within the summation will return a meaningful value. As τ increases, the start (sample one) of trace two becomes farther displaced from the start of trace one. This causes the samples of the first trace in the displacement range before τ to be multiplied by zero. With increasing displacement of y_k, the quantity of non-zero products within the summation decreases until the final summation where the only non-zero product is the last data point of x_k multiplied by the first data point of the y_k.

$$\phi_{xy}(0) = x_1 y_1 + x_2 y_2 + \ldots + x_{end-1} y_{end-1} + x_{end} y_{end}$$

$$\phi_{xy}(1) = 0 + x_2 y_1 + \ldots + x_{end-1} y_{end-2} + x_{end} y_{end-1}$$

$$\phi_{xy}(\tau_{max} - 1) = 0 + 0 + \ldots + x_{end-1} y_1 + x_{end} y_2$$

$$\phi_{xy}(\tau_{max}) = 0 + 0 + \ldots + 0 + x_{end} y_1$$

DATA

Frequency Analysis

A Fourier analysis (Fig. 4) using the SeisLab toolbox in MATLAB (Rietsch, 2022) shows the frequency content peaks between 5 and 10Hz and the amplitude exponentially decreases after. The data from all nodes for the duration of the record were stacked and used for the frequency analysis. All data used were not down sampled for analysis or processing.

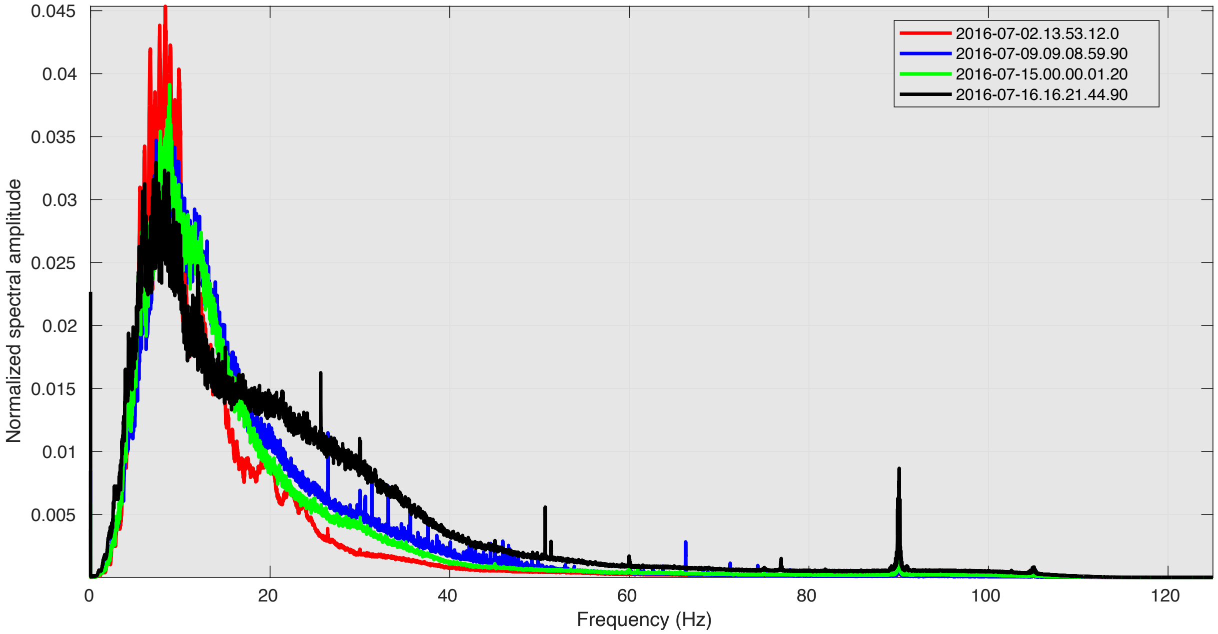

Figure 4: Frequency analysis of the four earthquakes showing a high content surrounding 10Hz and a spike at 90Hz, which is likely a spurious frequency or resultant self-noise phenomenon. Data from all nodes were used for the analysis.

Earthquake 198 (July 16), black in the figure, is the exception and the frequency content decreases at a different trend. This could be explained by being the furthest from the array or how the seismic waves propagate through the local geology. The basin shelf depth is shallower to the north and earthquake 198 may also be associated with the Nemaha fault or its seismic waves may be propagating though the fault. All events show a spike at 90Hz with a negligible influence on the final process determined by processing the data with and without filtering the low amplitude content. No explanation clearly explains the presence of this spike but it may be a spurious frequency. Because a correlation is the summation of series, it will override the influence of high frequency noise. The low magnitude earthquakes also produce little long wavelength energy and the short source-receiver distance renders these a non-issue. Applying a high pass or band pass filter to remove an inconsequential amount of data may distort the target data in the 5-10Hz range. After testing several filter types and frequency ranges, the effects of filtering were determined to remove too much content from the product and were not included in the final process.

Array and Instrumentation

The 2016 Community Wavefield Experiment array, located in Grant County approximately 3km. north of the Garfield County border, and was composed of three major parts: 1 east-west line and 2 north-south lines of nodes, a gradiometer array, and 6 triangular arrays of broadband and infrared stations (Sweet et. al, 2018). The component used in this study was the east-west line of 129 nodes spaced 100m apart (Fig. 2). The instruments used in this line were second generation Fairfield Nodal Z-land 3 component 5Hz nodes. These nodes were deployed between June 21-23, 2016 and retrieved July 25-27, 2016, recording for approximately 1 month at a sample rate of 4ms (Ringler et. al, 2018).

Compared to other, more traditional seismometers, the Z-Land nodes offer some advantages. Their per unit cost is low enough to deploy them in large enough quantities for a Large N array. An internal battery reduces the deployment footprint and carrying weight. In addition, their form is small enough to carry multiple at a time, and with no screw ports contacts, there is little worry of external elements entering the housing. Their self-noise tested above ambient above 30Hz and a sensitivity at 60Hz. This sensitivity may be a partial cause of the 90Hz spike seen in Figure 4.

Regarding instrument response, when data from different instruments are used together, removing the response removes signal distortion related to the instrument's mechanisms. This results in a signal that is true to the ground motion and can be compared to the signal from other measuring devices (Mosher and Audet, 2018). Because the instruments used here are the same and have been tested to have to have no significant differences between each node, there is no reason to remove the response from the Z-Land nodes.

Earthquake Characteristics

Four earthquakes selected from the deployment duration are referred to by their Julian day (184, 191, 197, 198). These have a magnitude of 2.8 to 3.0 and are 9 to 48km from the array. Only the vertical channel will be used from the nodes. Earthquake 184 originated 9.7km east of due south of node 1129. The arrival has western dipping arc with a polarity shift (Fig. 17, 18) and larger amplitudes to west. Because this earthquake was very close to the array, only the first multiple is clear (Fig. 5). The second multiple is present but is less defined than in other earthquakes and has no clear end. Earthquake 191 originated 33.5km west by northwest of node 1001 (Fig. 7), has a linear arrival dipping to the east, and up to 4 multiples identifiable in the original data. Earthquake 197 originated 31km due south of the middle of the array resulting in a parabolic arrival (Fig. 9) and up to 3 multiples. This earthquake has a unique convergence of positive peaks that squeeze out a negative peak near the middle of the seismogram (Fig. 21, 22). This characteristic will affect the correlation trace and how it will perform. Earthquake 198 originated 38.25km northeast of node 198 and has a linear arrival with 3 identifiable multiples and 2 additional multiples that are partially visible across the seismogram (Fig. 11).

Each seismogram displays several multiples (Fig. 5, 7, 9, 11) spaced approximately 1 second apart and an S-wave arrival that obfuscates the data and ends the useful time window. The target time window for correlation is the first arrival and the first multiple (Fig. 6, 8, 10, 12). Earthquake locations affects the appearance of the first arrival and determines how to manipulate the data for processing. Note that some traces were too noisy to use for the duration of the recordings and have been removed.

Closer earthquakes (184 and 197) show fewer multiples than the farther ones (191 and 198). Horizons in the seismograms are discernable with no processing but often diverge, are not continuous, or barely distinguishable from the surrounding noise. Whether these characteristics are a representative of the geology or a product of wave propagation is difficult to determine without additional seismic data or a comparison with a cross section from cores. The Anadarko basin shelf layers are nearly flat and mostly continuous on a state wide scale, excluding the deep basin, but will have faults and fractures and layer boundaries that refract and reflect seismic waves in ways that do not show ideal geometries.

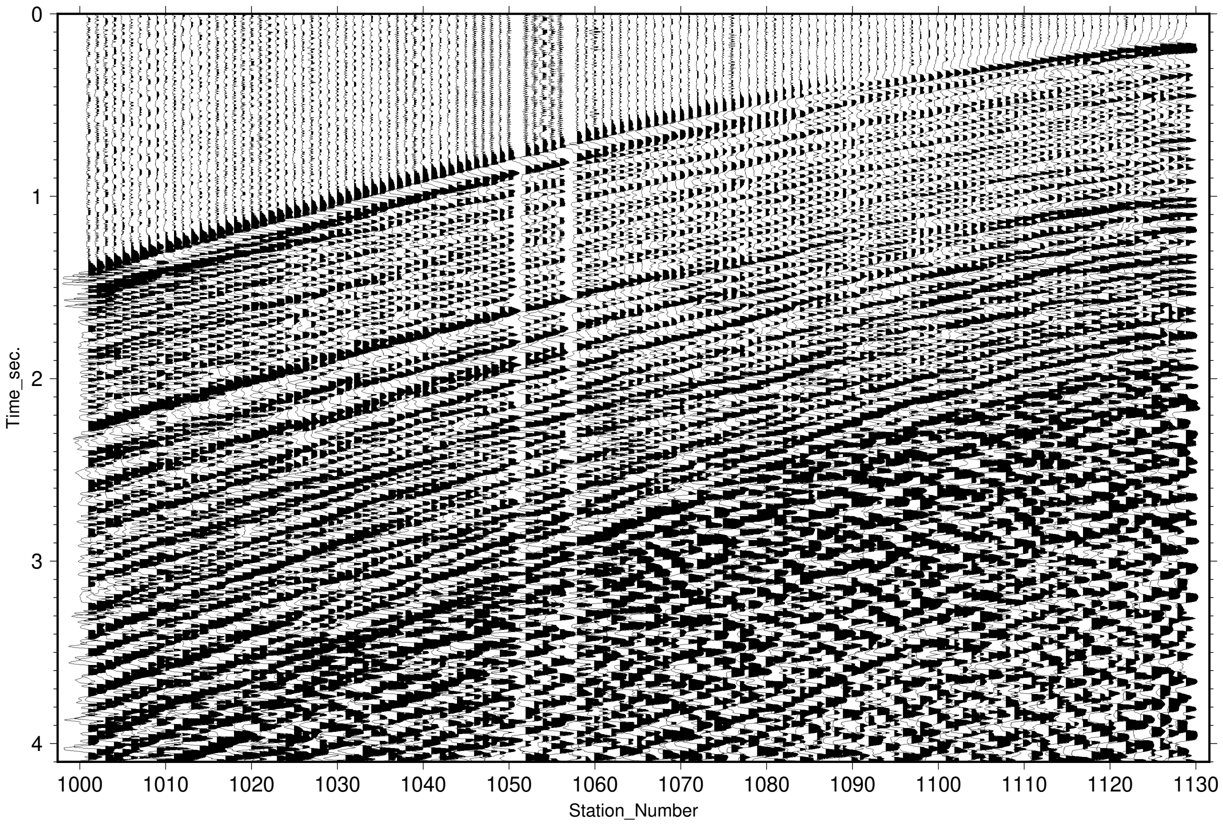

Figure 5: Original seismogram for earthquake 184 showing the full P-wave arrivals. Earthquake 184 was located approximate 10 km south of node 1129 and had a M_L of 2.8

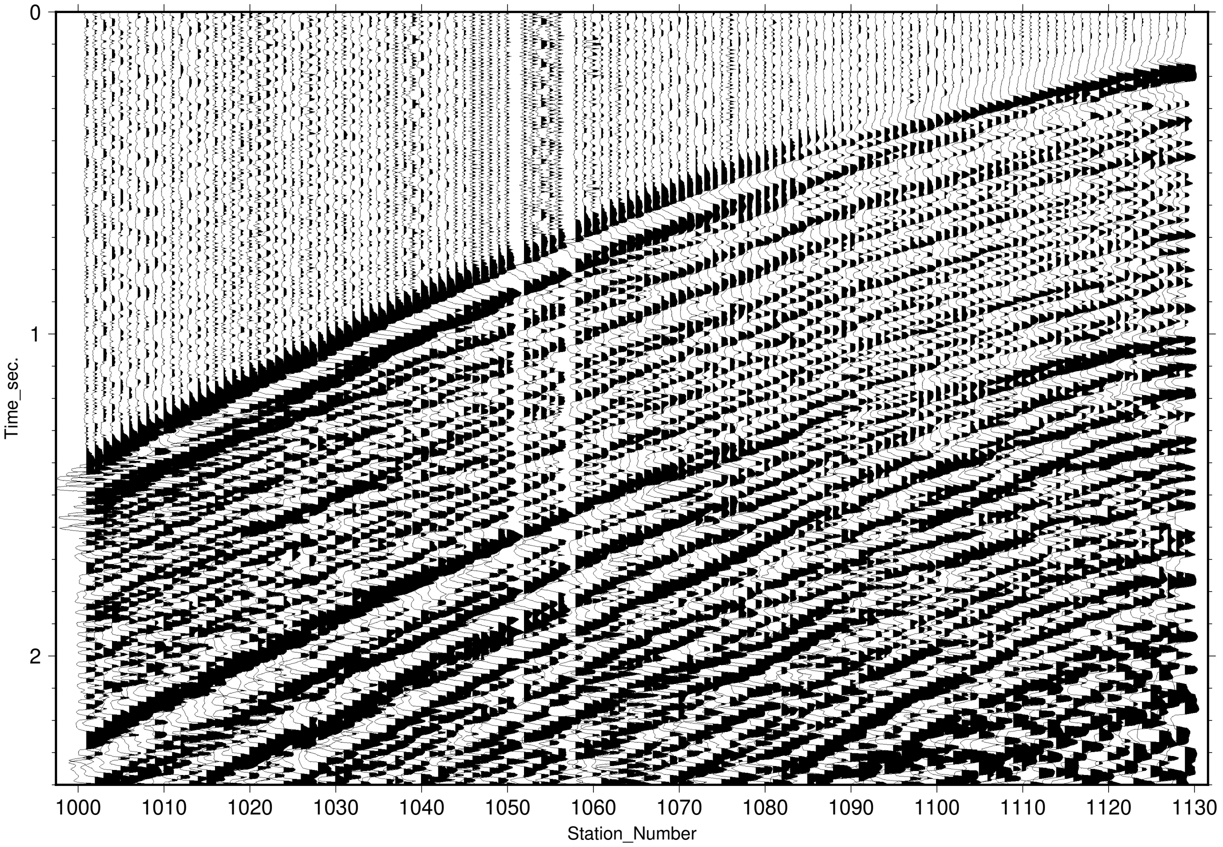

Figure 6: Seismogram with a window focusing on the first multiple of earthquake 184 before processing.

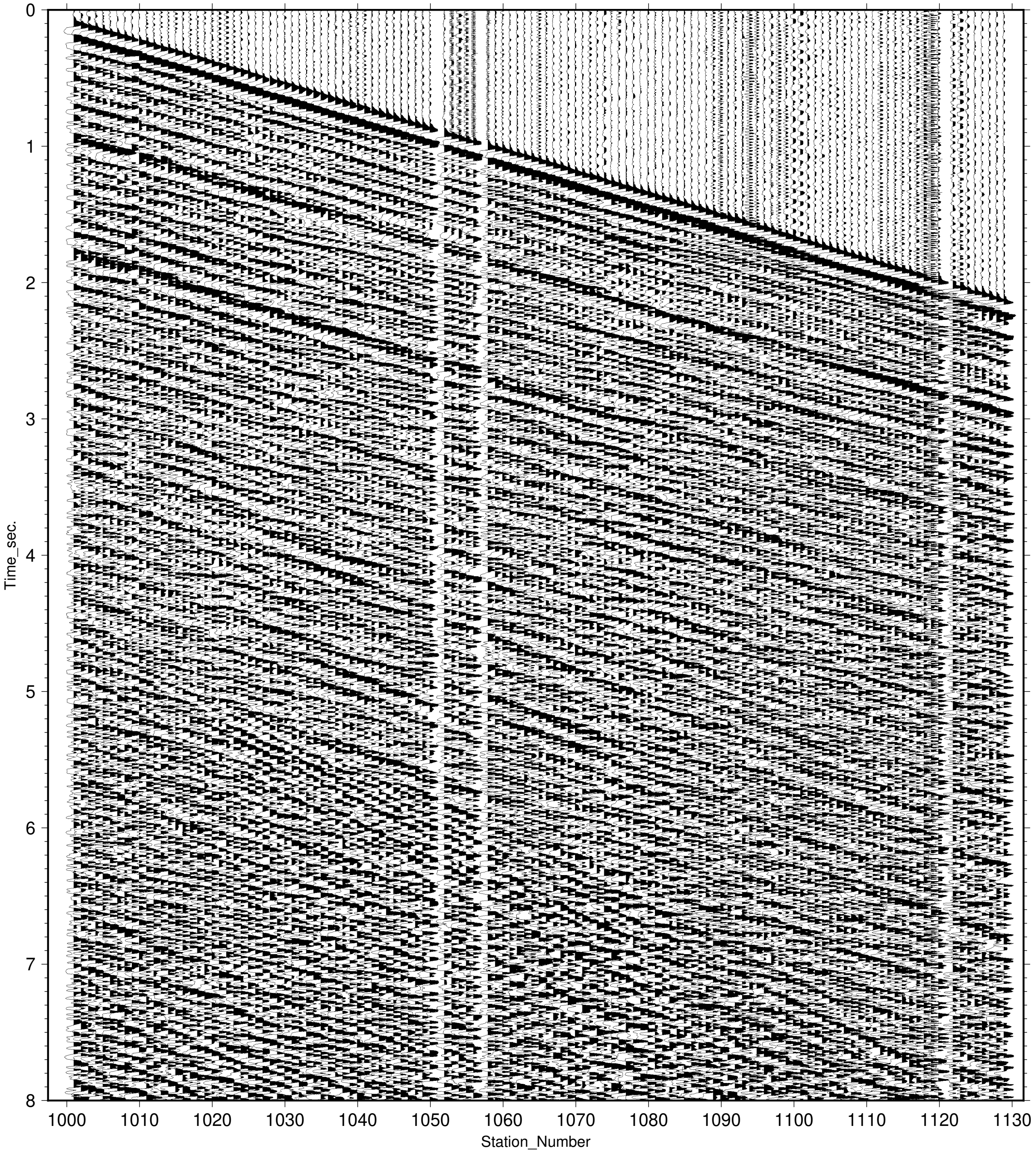

Figure 7: Original seismogram for earthquake 191 showing the full P-wave arrivals. Earthquake 191 was located approximately 34 km northwest of the array and had a M_L of 3.0.

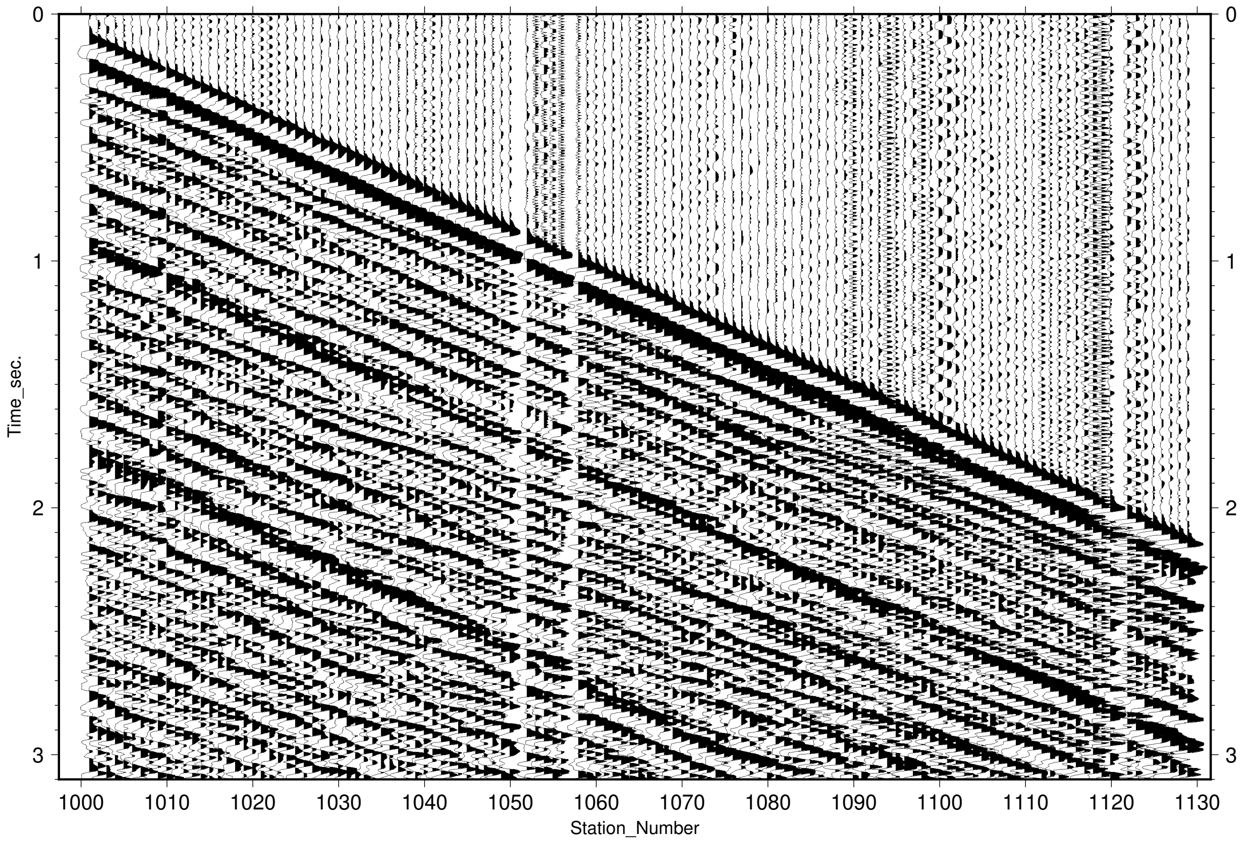

Figure 8: Seismogram with a window focusing on the first multiple of earthquake 191 before processing.

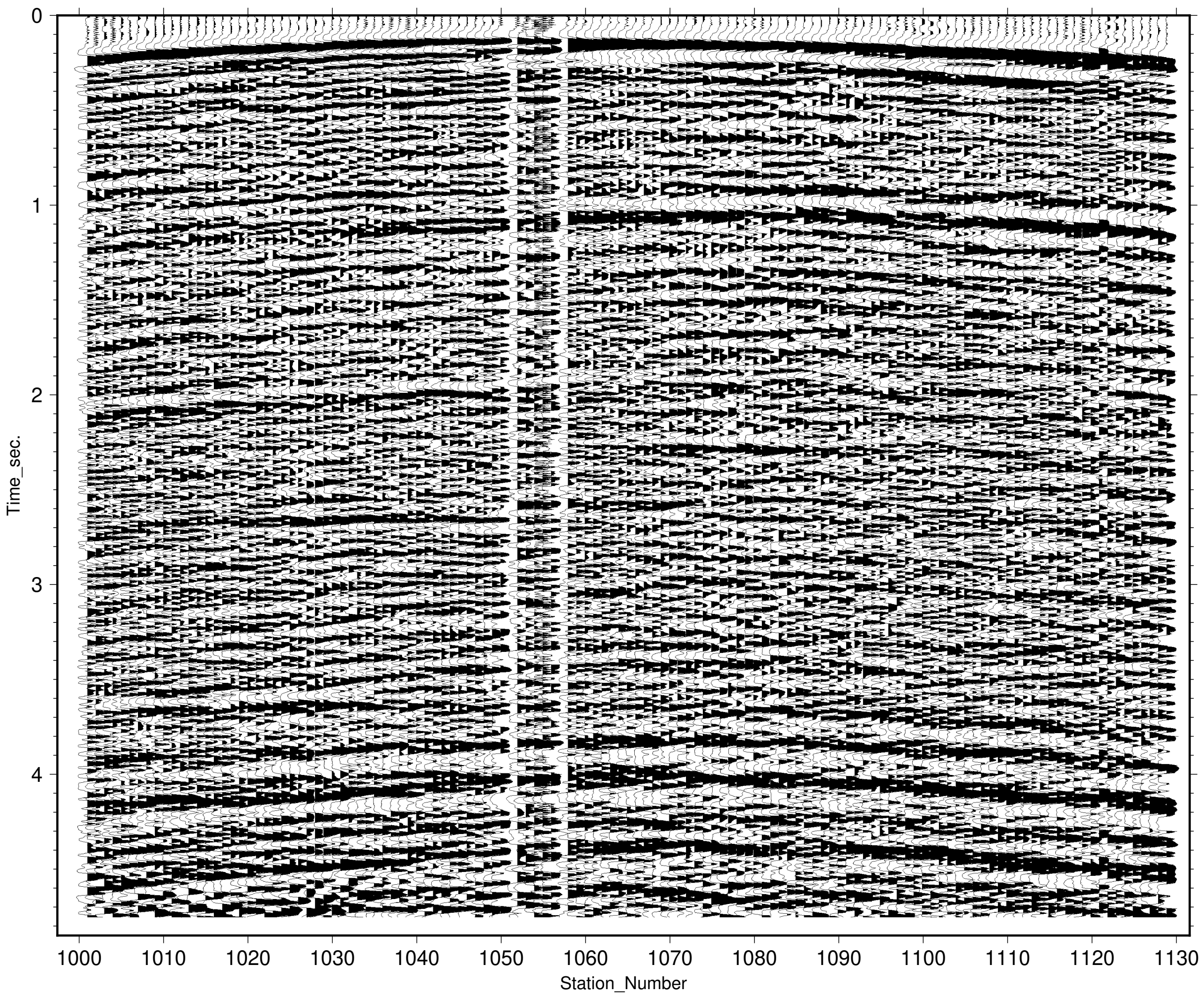

Figure 9: Original seismogram for earthquake 197 showing the full P-wave arrivals. Earthquake 197 was located approximately 31 km due south of the array and had a M_L of 3.0.

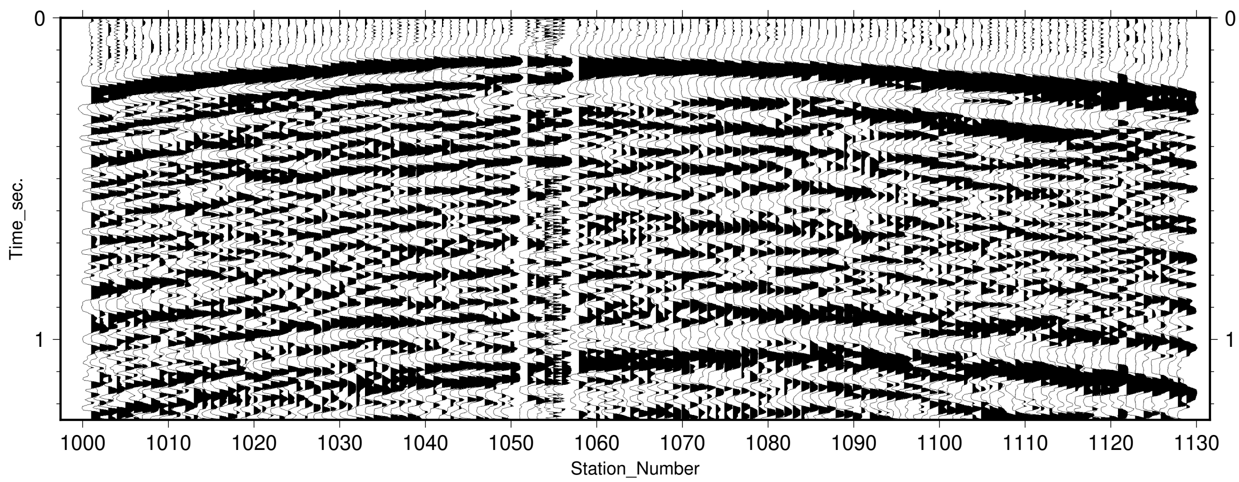

Figure 10: Seismogram with a window focusing on the first multiple of earthquake 197 before processing.

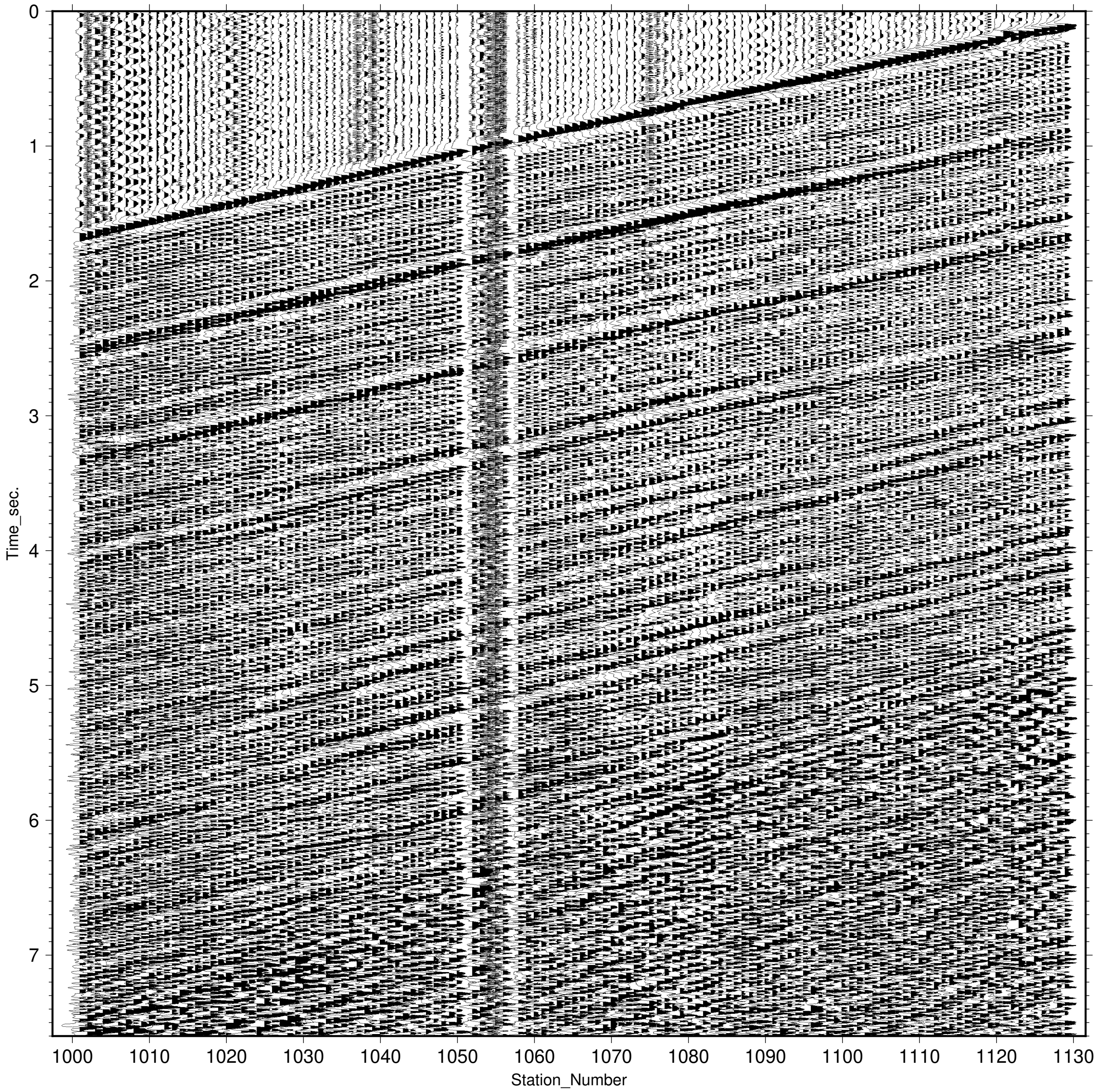

Figure 11: Original seismogram for earthquake 198 showing the full P-wave arrivals. Earthquake 198 was located approximately 38 km north east of the array and had a M_L of 3.0.

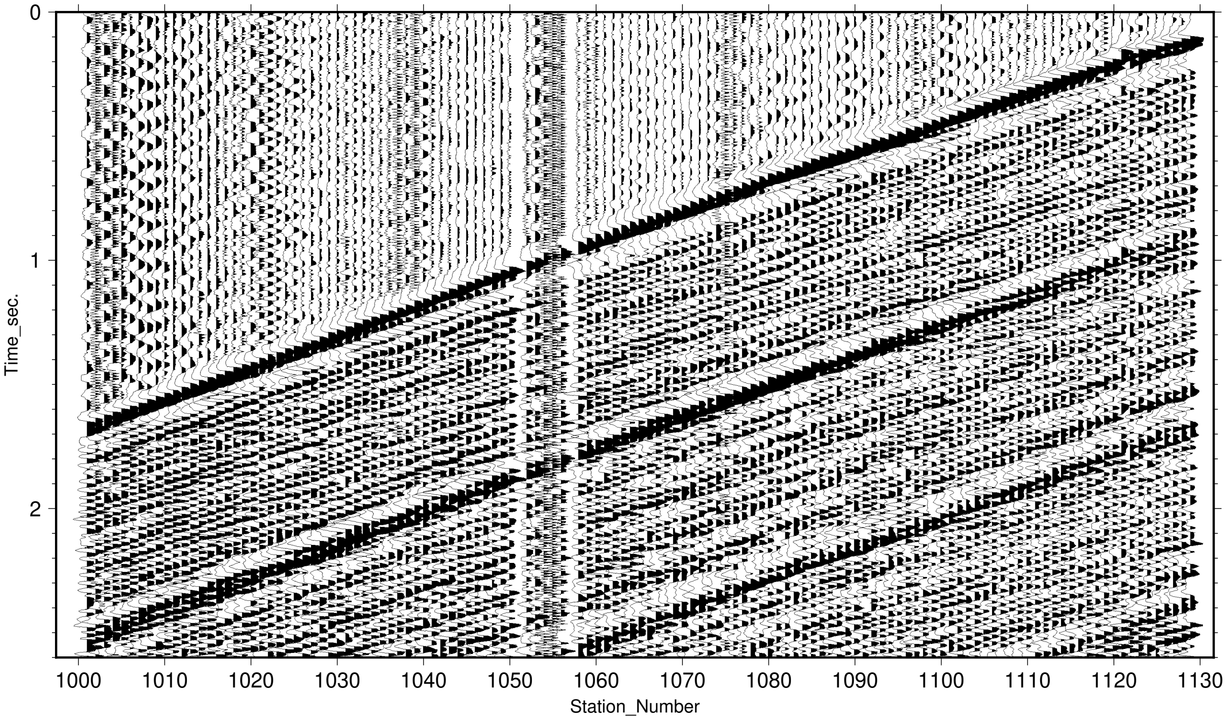

Figure 12: Seismogram with a window focusing on the first multiple of earthquake 198 before processing.

METHODS

Overview

A partial autocorrelation requires three major processing steps. The first is preprocessing that includes file type conversion and ensuring earthquake properties and geometry are calculated for the file. The second step is isolating the information of interest and has two parts: Preparing the data to be correlated through windowing, muting, and reducing the velocity, and using the same methods to extract the traces that will be used to correlate the seismogram. This file is what differentiates this partial autocorrelation from a traditional autocorrelation or cross correlation. The final processing step is the correlation itself, which uses the cross-correlation function in Seismic Unix. The correlation will use the first arrival and focus on the effect on the first multiple. This results section will skip the first group of steps (conversion through trace elimination) and progress though the second and third parts then discuss the final products.

Processing

The correlation methods presented are partial autocorrelations. Rather than autocorrelating the whole seismogram with its self or cross correlating the seismogram with a single trace, this method cross correlates the seismogram with the first arrival. As discussed previously, our goal is to translate the hypocenter from depth at a distance away to a closer virtual source based on the first arrival geometries. By doing a partial autocorrelation on the first arrival, the P-wave multiple become more pronounced with the secondary effect of improved signal to noise ratio. This is done two ways: by setting the cross-correlation file to the first impulse or setting the cross-correlation file to the first set of multiples. The former scenario works well on all seismograms and the latter works well when groups of multiples are visually identifiable. Both will be discussed in the Interpretation section.

All seismic data processing was done in Seismic Unix (Stockwell, 2019) and scripted using Python 3. The script work flow, summarized in Table 1, uses standard functions and is focused on manipulating the data to be correlated with minimal trace distortion. The SEGY files are first converted to SU format and separated by component. Source locations are added to each SU file as longitude and latitude in decimal degrees then converted to UTM coordinates. The small distances between sources and receivers allows the nodes and sources to be represented on a rectangular grid. This greatly simplifies source to node geometries and calculations. After conditioning the data for use within Seismic Unix, the data can now be manipulated and correlated. Many of the optional steps in the table are for testing their effect on the final product and may be useful on complicated data sets (more noise, irregular node placement, etc.). A step being optional only means that the script can continue piping data to the next processing block if it is not executed. The entire process will not function as needed without several of them.

Table 1: Table of all functions used and available during the correlation process. Each row describes the Seismic Unix functions, the processing order and command group in the Python script, and if the step can be skipped. Final images are plotted using Generic Mapping Tools 6.

Function	Optional	Description
Prepare	N	Convert to SEGY to SU, sort and split by component, modify headers
Utmconv	N	Add source coordinates, convert to UTM, apply scaling
Azimuth	N	Compute source azimuth and node offset
Filt	Y	Apply filter to seismic files
Kill	Y	Kill noisy traces
Reduce	Y	Apply velocity reduction to flatten the first arrival slope
Mute	Y	Apply null values to sections of the seismogram
Window	Y	Isolate sections of the seismogram
Corr	Y	Select crosscorrelation file and apply the correlation
Gain	Y	Apply a gain to the correlated file
Sutosegy	Y	Write header information and convert SU back to SEGY
Gmtplot	Y	Plot the end product using GMT

Data Manipulation and Selection

The purpose of windowing the data is to improve readability and save computing resources. All earthquakes have several multiples before the S-wave arrival. Multiples after the first two have lower energy and become noisier. They do not have a meaningful impact on the correlation product but add noise to it. Windowing is used to remove that extra trace length. Another consideration is that muting alone serves the same function of removing unnecessary data but does not remove the null trace data. Applying a window and mute curves produces the cleanest results but requires drawing a muting curve by hand. This can be tedious and often is not necessary. Velocity reduction serves a similar function to effectively reducing the length of the window and improves readability of the results. A reduction can be applied before or after the correlation but reducing the seismogram before eliminates the need to draw detailed curves needed for correlation trace selection and muting. Because of these reasons a reduction will be applied first causing the earthquakes now have a near flat first arrival. The input for these reductions were the full P-wave seismograms from the data section (Fig 5, 7, 9, 11) and result in the following images (Fig. 13-16). The reduction velocities for earthquakes 184, 191, 197, and 198, in km/s, are 6.6, 6.15, 6.0, and 6.0 respectively.

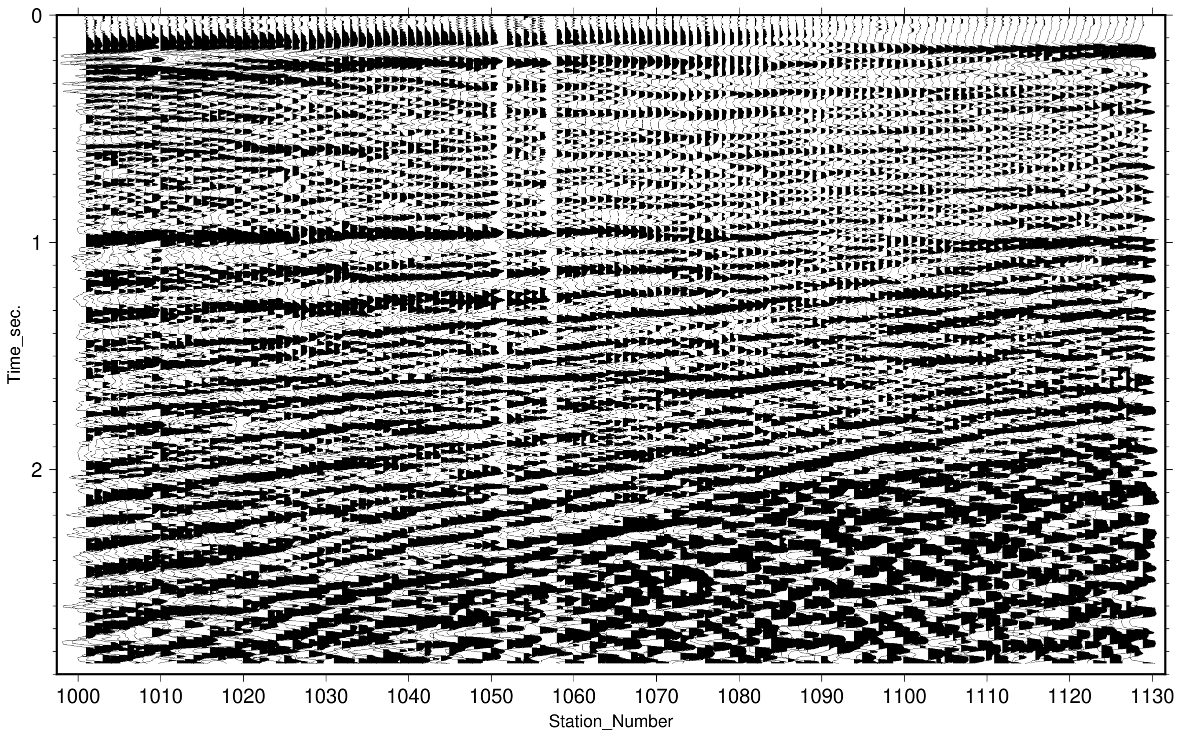

Figure 13: P-wave section of earthquake 184 (Fig. 5,6) after a velocity reduction at 6.6 km/s. Because velocity reduction is a linear process, the second multiple is drawn out and shows no distinct conclusion.

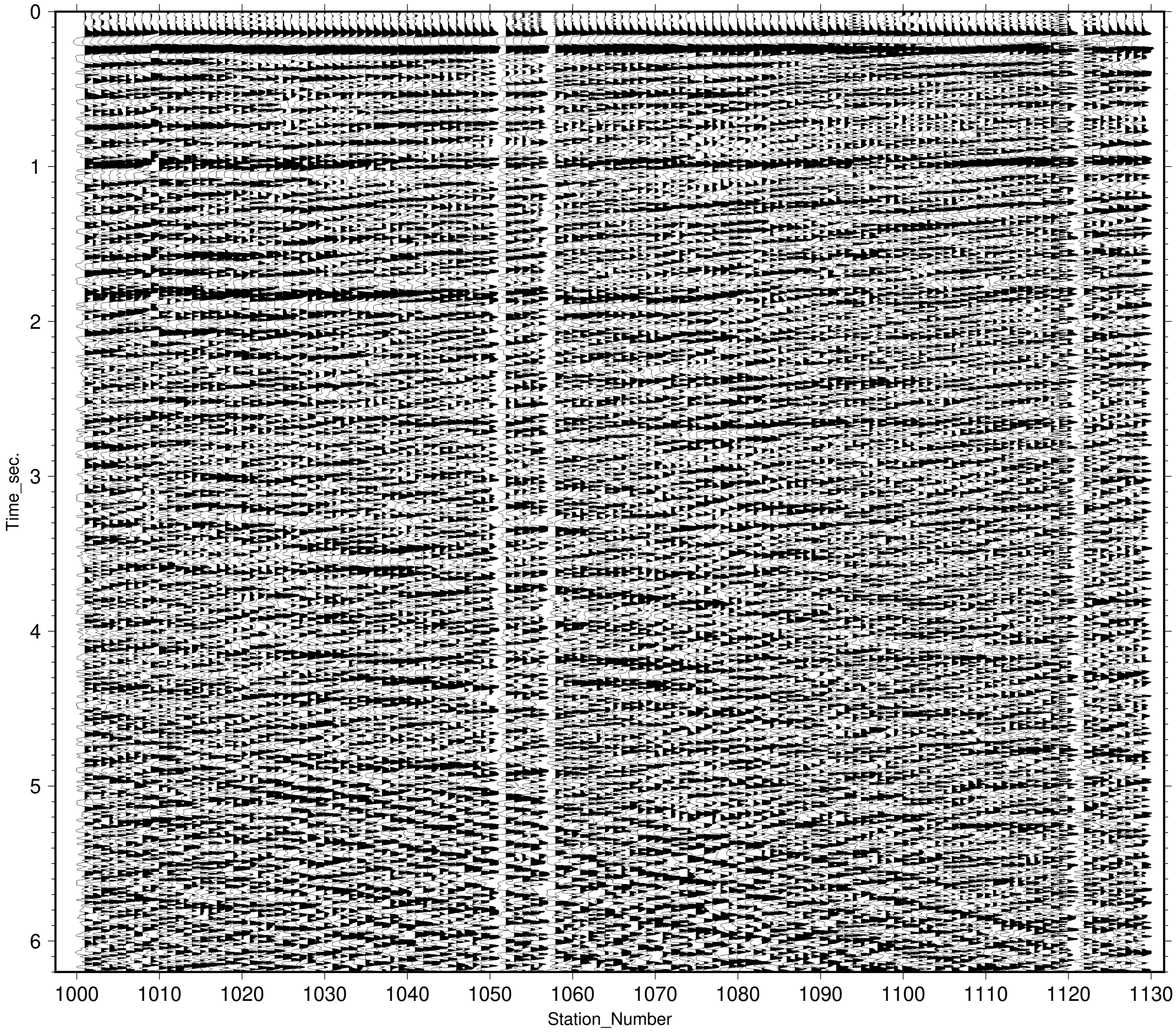

Figure 14: P-wave section of earthquake 191 (Fig. 7,8) after a velocity reduction of 6.15 km/s.

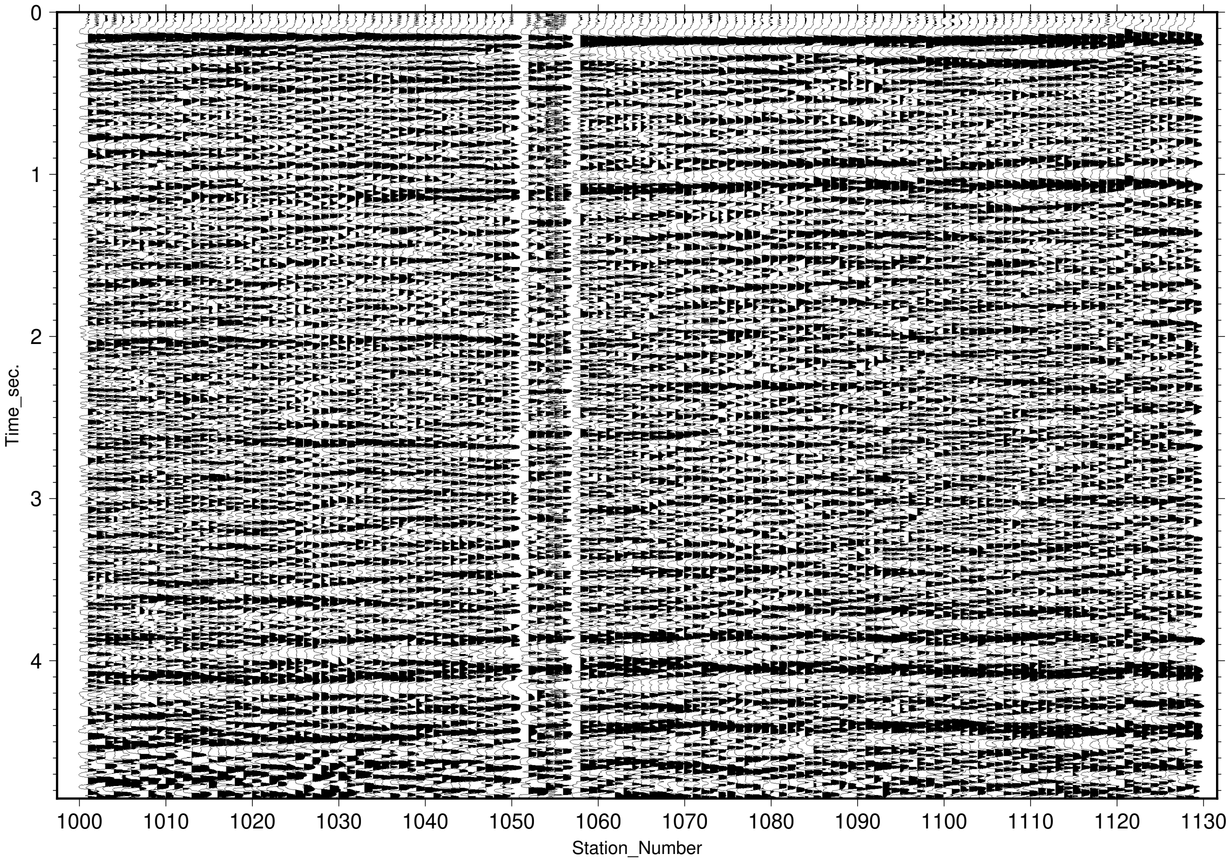

Figure 15: P-wave section of earthquake 197 (Fig. 9,10) after a velocity reduction of 6.0 km/s. Unlike earthquake 184, the velocity reduction on earthquake 197 resulted in an even raise in arrival times. The parabolic trend is more visible after 3 seconds but has no distinguishable multiple markers.

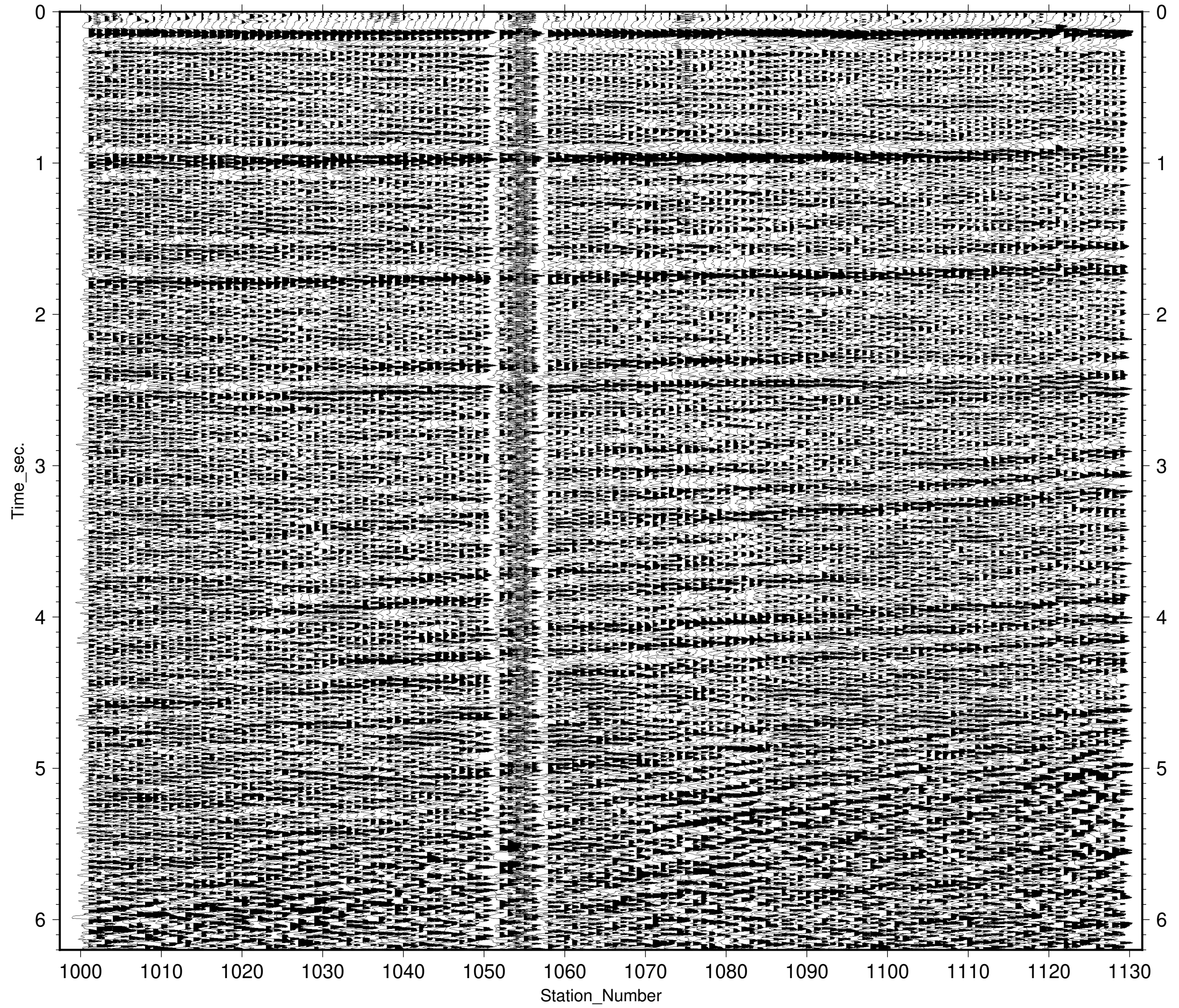

Figure 16: P-wave section of earthquake 198 (Fig. 11,12) after a velocity reduction of 6.0 km/s. The effects of the reduction wane after the second multiple and become apparent after 3 seconds.

The correlation trace is the most influential component of the correlation. Autocorrelation runs a trace from an array trace against itself. Cross-correlation runs one trace against all other traces. This trace comes from the first arrival across the entire array from all stations instead of segment from one station. For this purpose, the first arrival is not just the first positive or negative peak. It should be in the form of a Ricker wavelet with a positive-negative-positive or negative-positive-negative for. Adding more than a three peak wavelet decreases the visual improvements. The first one second of each earthquake are shown in Fig. 18, 20, 22, and 24 were used to manually extract the correlation traces shown in Fig. 17, 19, 21, and 23. To maintain consistent processing for each event, the length of trace segments for the correlation must be consistent and was done by adding a static amount of time to the starting curve. Because the first arrivals may not be entirely flat, some of the wavelet may be clipped. This didn't not affect the final correlation. Extending the trace window to include the full wavelet and other potential data resulted in a muddled correlation.

Two earthquakes with a non-linear arrival are special cases that make selecting a correlation trace difficult. The first is earthquake 184 (Fig 17-18) where the first arrival polarity switches between nodes 1085 and 1095. For this seismogram the first arriving P-wave at station 1129 was used to set the window limits. The second is earthquake 197 (Fig 21-22), located directly south of the middle of the array, which resulted in a parabolic arrival. From node 1001 to node 1155 two positive peaks converge and over a negative peak that would otherwise be present across the seismogram. At node 1100 and continuing east the positives begin to separate again. This compression could be caused by a layer discontinuing near that area or from the difference in travel times. The perpendicular ray path from the epicenter to the middle of the array may also bypass the layer. These deviations from the ideal wavelet form cannot be worked around and must be considered when analyzing the data. A reasonably clean correlation trace can be extracted from the other seismograms. Because correlation is a sum of products, when the likeness is a negative peak passing over a negative peak, the resulting product will be a positive peak as show with earthquake 184 (Fig. 17, 18).

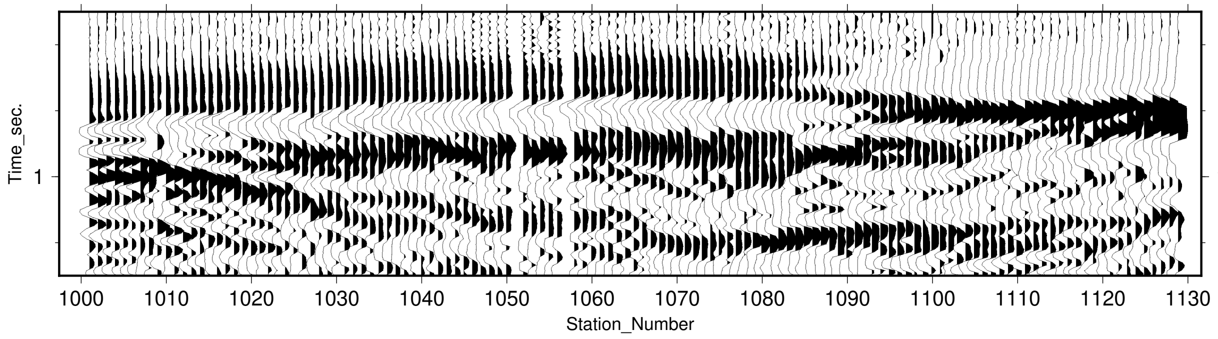

Figure 17: First arrival wavelet of earthquake 184 showing the wavelet that will be extracted for the correlation trace, including the polarity shift.

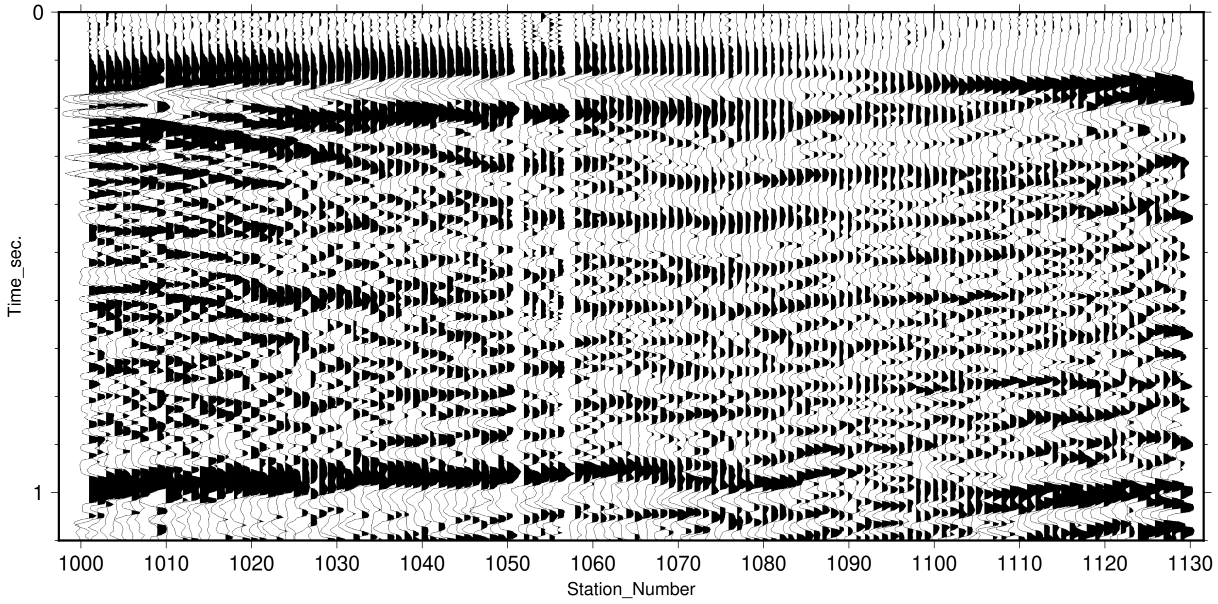

Figure 18: The first 1 second of earthquake 184 showing the first multiple and polarity change surrounding node 1190.

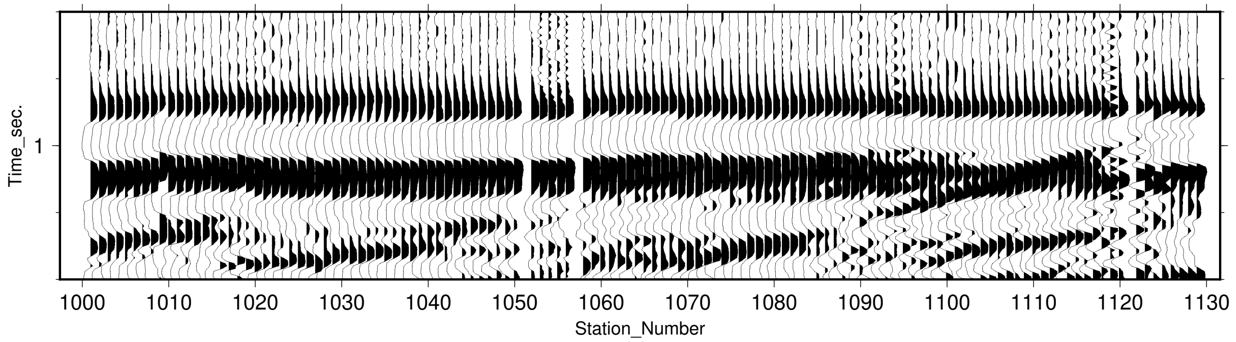

Figure 19: First arrival wavelet of earthquake 191 showing the positive-nevative-positive wavelet that will be extracted for the correlation trace.

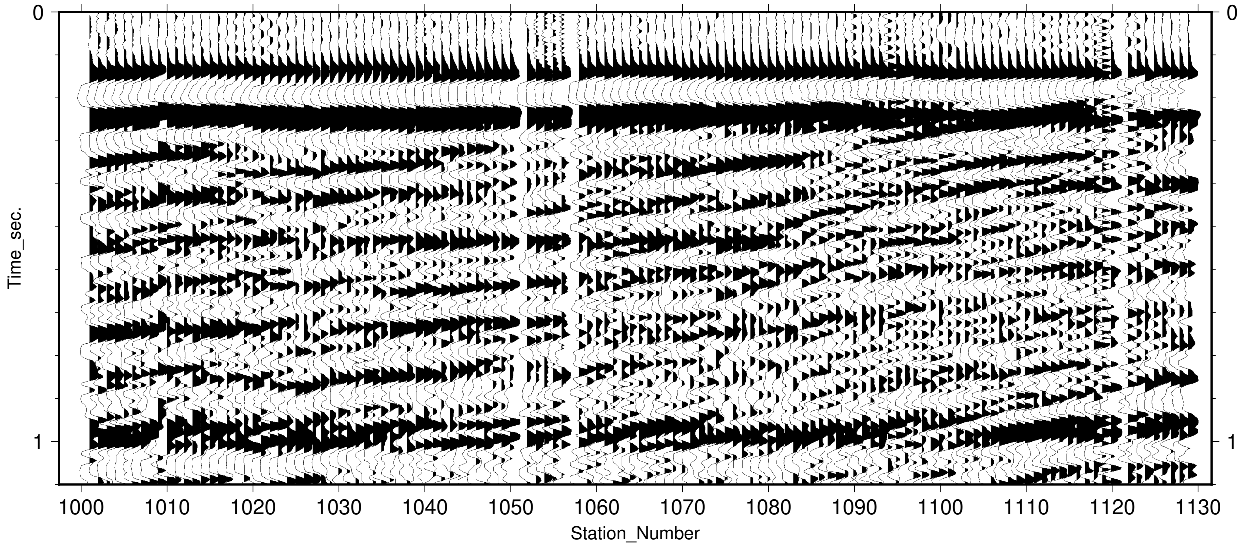

Figure 20: The first 1 second of earthquake 191 showing the first multiple.

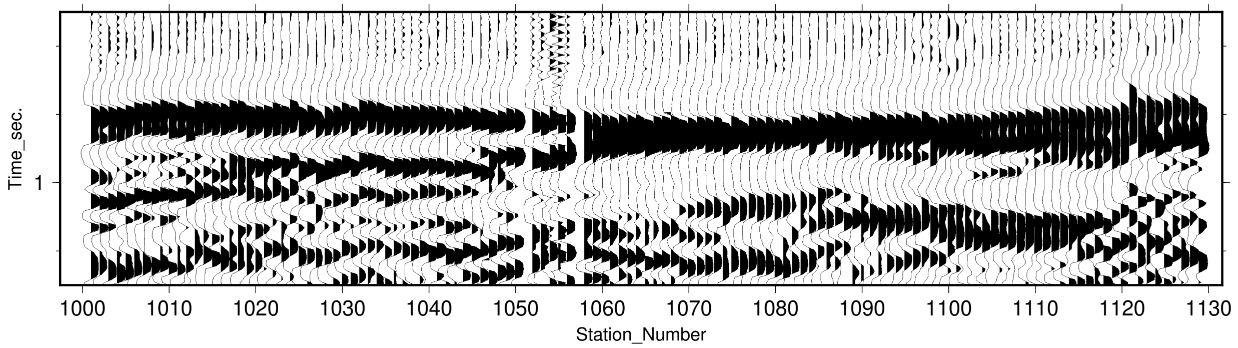

Figure 21: First arrival wavelet of earthquake 197 showing the negative-positive-negative wavelet that will be extracted for the correlation trace.

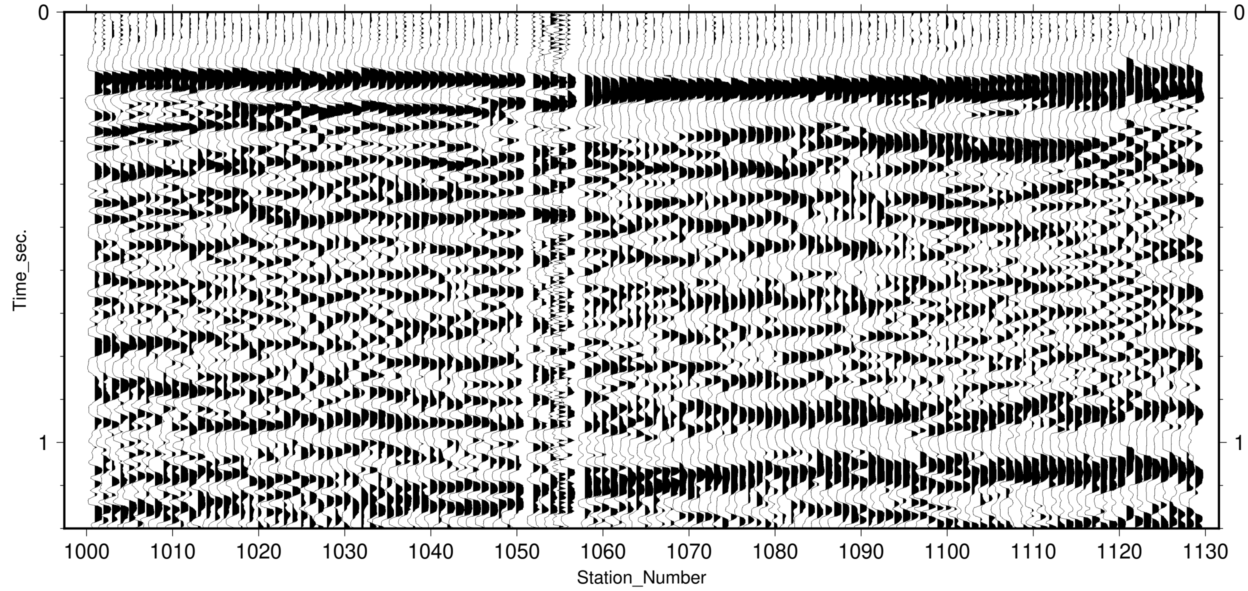

Figure 22: The first 1 second of earthquake 197 showing the first multiple and converging positive peaks between nodes 1055 and 1110.

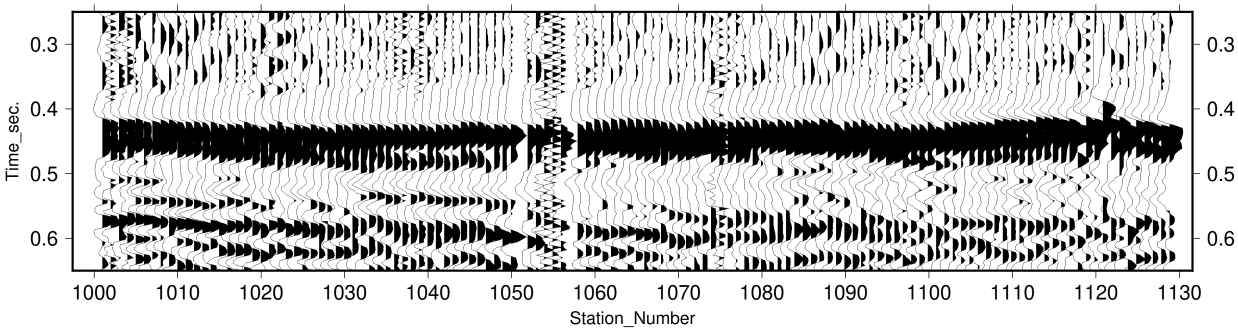

Figure 23: First arrival wavelet of earthquake 198 showing the negative-positive-negtive wavelet that will be extracted for the correlation trace. The branching positive peaks at 0.45s will be included as part of the positive peak of the wavelet.

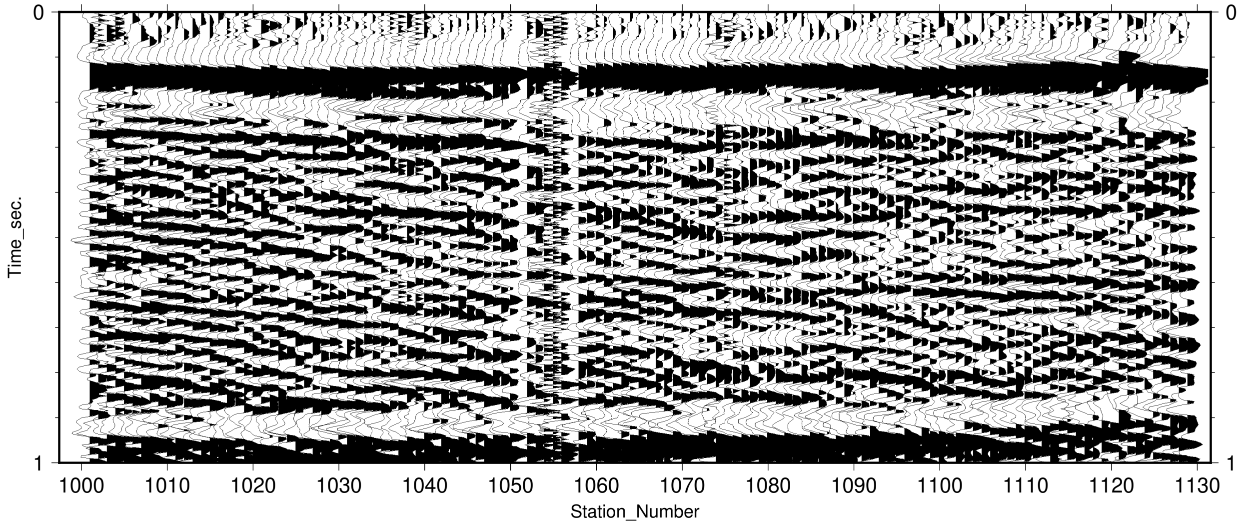

Figure 24: The first 1 second of earthquake 198 showing the first multiple.

At this point the seismograms have been flattened and windowed to include all P-waves, and the correlation traces have been extracted. Using the first time of the trace correlation window, everything above the that time in the seismogram will be muted. Muting can also be used to remove any additional trace data past the first multiple if preferred. However, matching horizons from the first and second multiples of the correlated seismogram adds a level of verification that can be used. The shorter times between multiples and additional noise present in later multiples as seen in earthquake 198 do not respond as well as the first and second multiple to the correlation trace that was pulled from the first arrival. Earthquakes 191 and 197 show the opposite where the horizon indicators are at least partially visible and continuous. The correlation should clarify these seismic horizons.

A limitation of Seismic Unix is being unable to set non-rectangular seismic windows, which is a result of the requirement that all seismic traces in a SU or SEGY file have the same length. Non-rectangular windows, in this context, are time limited widows of a recording that do not have the same start and end time for all traces. An example of this would be the unprocessed seismogram of earthquake 191. Drawing a rectangle at the start of the first trace would include ambient noise before the first arrival of the last node. Also, the industry-wide assumption is that all traces in SEGY file begin at the same time, this is because early seismic recording instruments began all traces at the same sample interval allowing for sample skew; that all recordings start at the same time and traces have the same length but the wave arrivals are at different times, resulting in a non-rectangular seismic window. However, the existence of SUREDUCE to accommodate seismic refraction violates this assumption by shifting traces based on a seismic velocity (Table 2). This forces the data into a rectangular form. Using the data as-is allows noise to enter the calculations making the product less meaningful and improving processing time. To mitigate this limitation, a combination of velocity reduction, muting, and windowing can be used to shift the seismographs into a rectangular window with minimal distortion. The first method uses velocity reduction to remove a progressively increasing amount from each trace as node offset from the source increases, resulting in a squared up seismic section than can be windowed easily. The second method uses a muting curve that traces just before the first arrival and the same curve at a user defined time distance later. Everything above and below the respective curves are muted and given a null value. This method does not flatten the arrivals in the seismogram and is useful for near horizontal seismograms or parabolic arrivals that are difficult to use velocity reduction on. Windowing this section is a just a convenience that limits the size of the final product. Because all values outside of the muting curves are null they will not affect the calculations. Windowing with this method will just reduce the file size make the product smaller. These processes are used with different time gaps to produce the correlation trace and the traces that will be correlated on.

Table 2: Table showing the reduction velocities of each earthquake. These velocities were used with SUREDUCE to shift the first arrivals upwards into a flat horizon.

Earthquake	Reduction Velocity (km/s)
184	6.6
191	6.15
197	6.0
198	6.0

CORRELATION RESULTS

Each earthquake has a unique form and characteristics that provides an example of how a partial autocorrelation will affect various seismic recordings. A quick summarization of each earthquake's original form is as follows. While reviewing the results, it is important to remember that while the correlation is a representation of the subsurface image, it is also a visual representation of the likeness of two signals. In this case it is the likeness between the first arrival wavelet and the subsurface. Because this method was derived to emphasize multiples from surface reflections, the strongest responses will be the multiple boundaries.

Regarding all correlated seismograms (Fig. 25-28), the most notable difference is the strengthened horizons. The first arrival and multiple separation horizons are the most clearly affected. Seismic noise has been reduced across all earthquakes and previously vague layer boundaries are more discernable. A consistent feature of all seismograms is some anomalous noise, or in earthquake 191, a cluster of westward dipping layers centered around node 1090. A correlation is the representation of similarities between signals. Clarifying the noise from earthquakes 184, 197, and 198 has mixed result and the group of dipping layers shown in earthquake 191 becomes more integrated into the seismogram. Multiples after the second were not clarified as much as expected based on the improvements of the first two. There is some marginal improvement but the shrinking multiple time gap did not correlate well. As expected, the correlation adds no benefit to the S-waves and they are not included in this discussion.

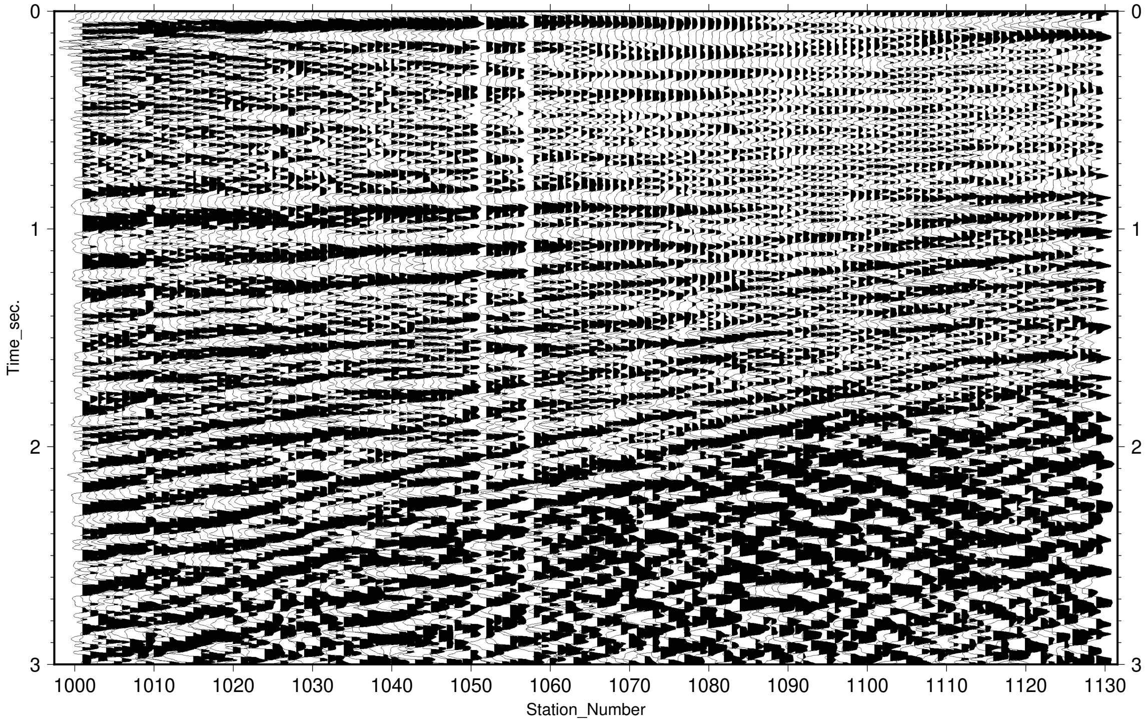

Figure 25: Correlated seismogram of earthquake 184 showing all P-waves. Velocity reduction successfully raised the western traces for the first ~1.5s. Because the arrivals were not linear, the function could not fully correct the signal that arrived slower than the function could accommodate.

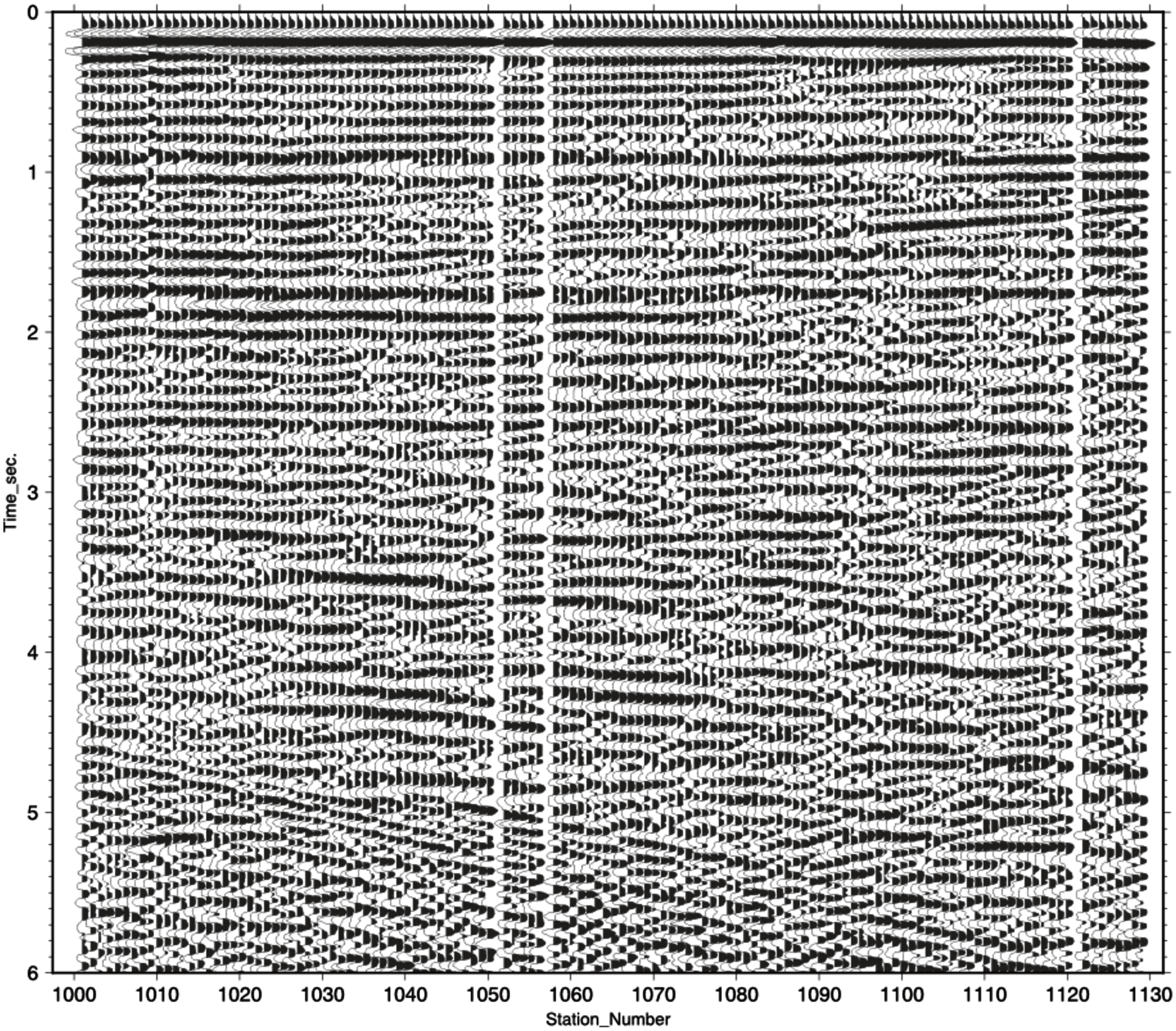

Figure 26: Correlated seismogram of earthquake 191 showing all P-waves. Multiples after the second are not clearly defined and the effects of the reduction fall off after about 2.5s.

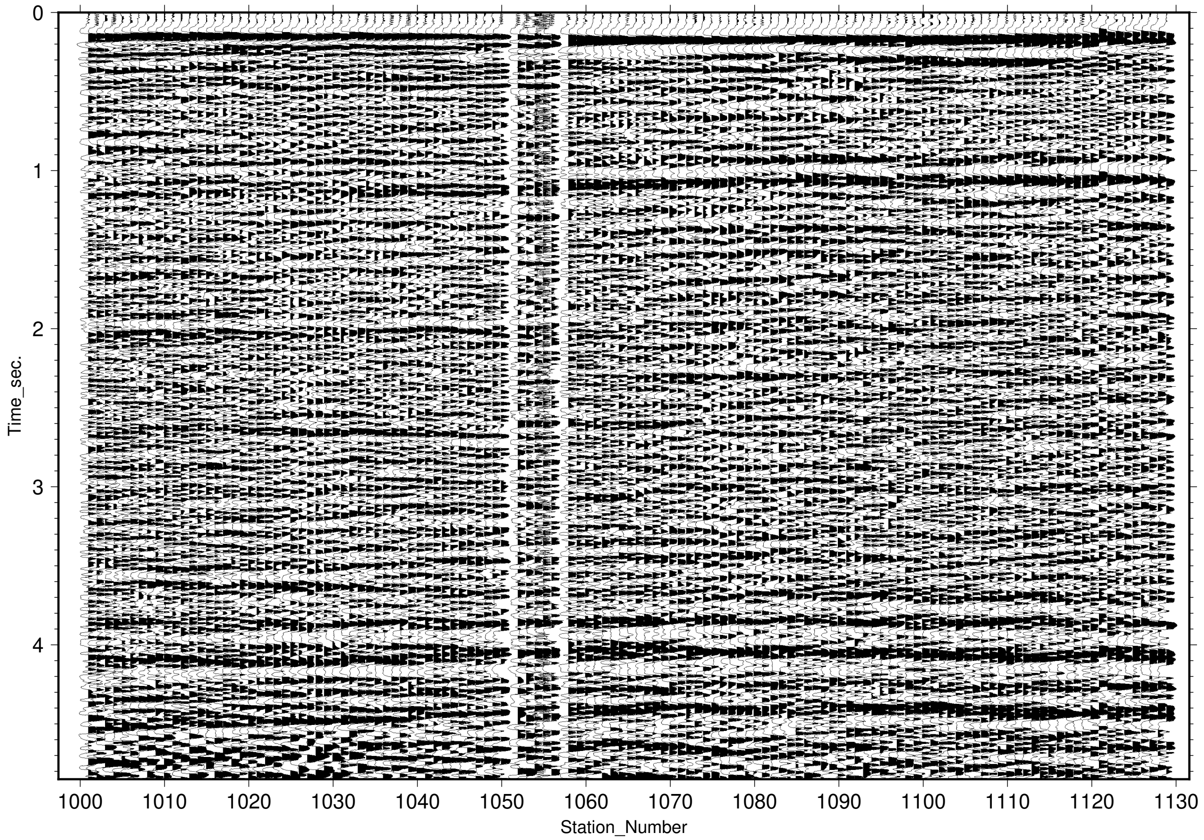

Figure 27: Correlated seismogram of earthquake 197 showing all P-waves.

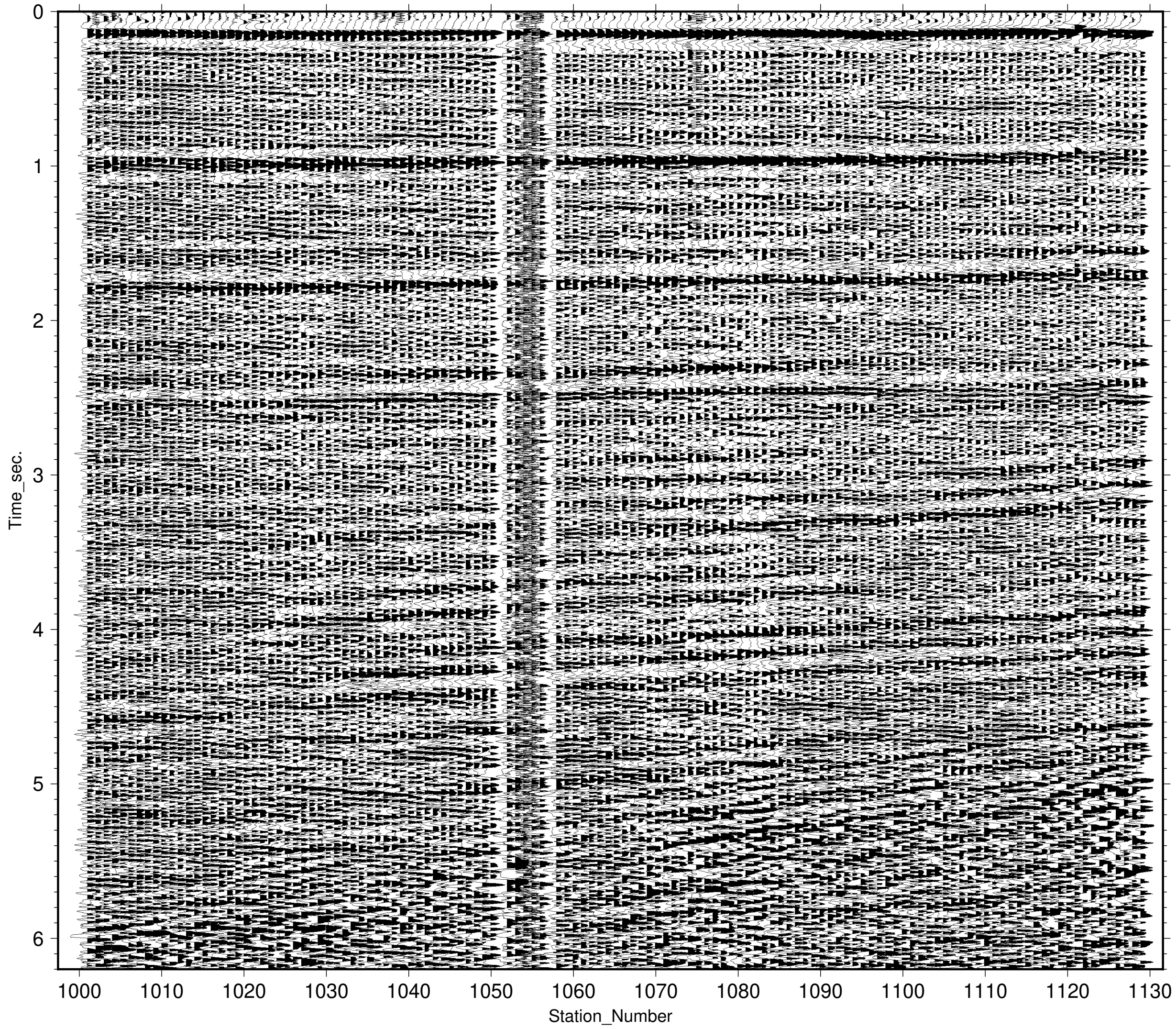

Figure 28: Correlated seismogram of earthquake 198 showing all P-waves.

Comparing the first two multiples from the reduced and correlated seismograms illustrates the changes better than a full view by itself. Starting with earthquake 184, the polarity shift between nodes 1090 and 1100 has not been removed entirely. The negative first arrivals on node 1100 to 1129 in the reduced seismogram have been transformed into positives due to the multiplication in the correlation formula, forming a more continuous first arrival. The phase transition did not have a strong positive or negative characteristic, resulting in a weak correlation resembling the noise seen in the reduced seismogram. Though the horizons in the reduced seismogram are thinner (e.g. 0.4s between nodes 1065 and 1085) compared to the correlated seismogram. The form of the horizons maintains consistency. Reflectors below 0.5s do not show significant improvement in correlation strength but the reduction of noise reveals them enough to improve visual clarity.

Velocity reduction shifted the first multiple to a horizonal position suitable for correlation. It could not fully compensate for the parabolic curve of the data. The increased time interval for the second multiple permits the correlation to work to some extent with correlations at the end of the seismogram. Differentiating where the second multiple ends is difficult, rendering the process not useful after the first multiple. Forcing a proper correlation would require application of several mute curves and possibly excluding the first multiple from analysis.

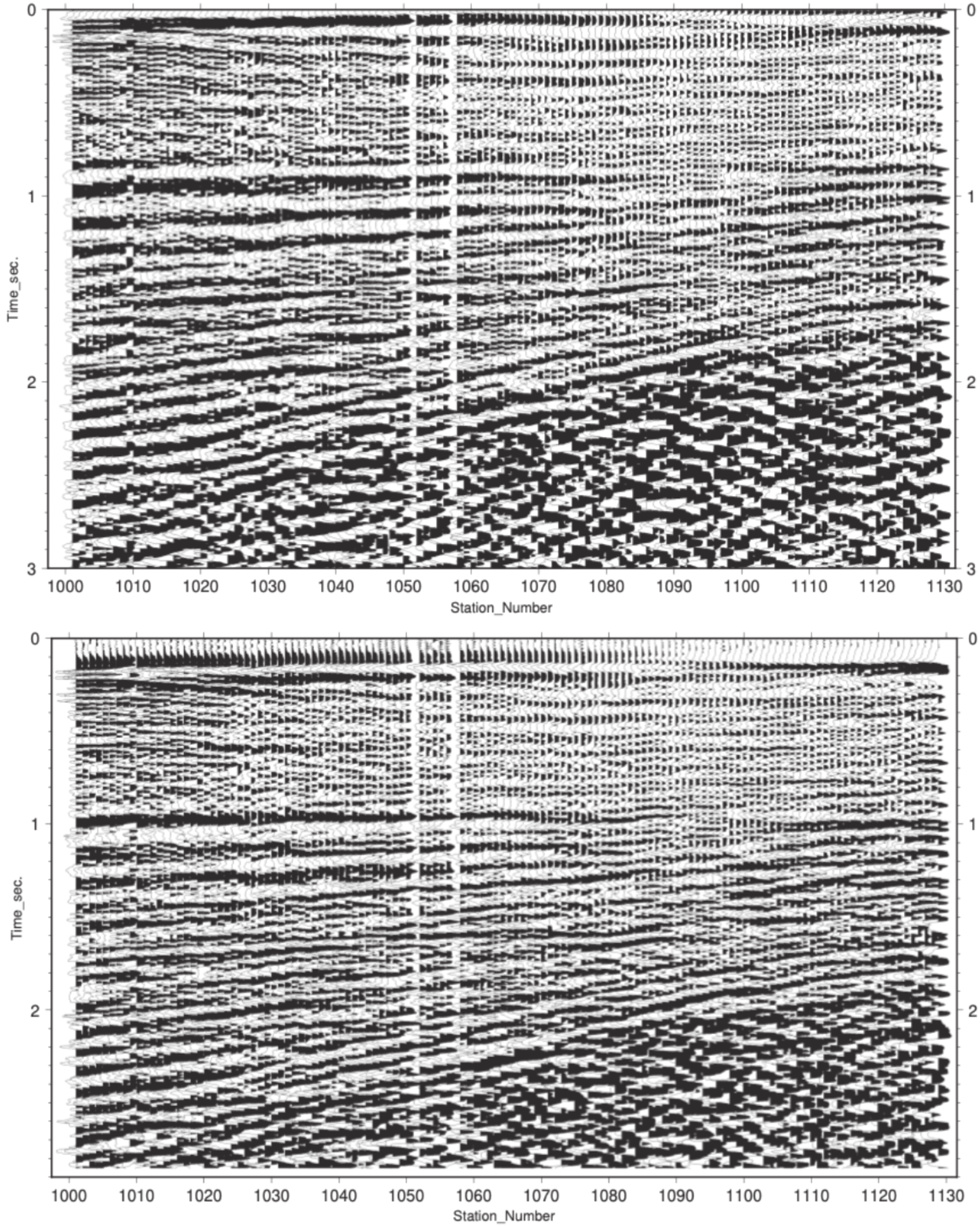

Figure 29: Earthquake 184 comparison of the first 2 multiples of the reduced seismogram (below) and correlated seismogram (above).

Earthquakes 191 and 198 have linear arrivals and can be discussed together. These two correlations also show the variations that can come from the same process used on similar seismograms. The most notable feature of the 191 correlation is the consistently high amplitudes of the reflectors through the whole seismogram. Using the first two multiple comparison (Fig. 30) we can see the horizons in the reduced image that are already visible have directly corresponding signals in the correlated image. The eastern reflections that were noisy have been strengthened and can now be connected to the western horizons. Between nodes 1080 and 1115 are the diffing layers. In the reduced image, it wasn't clear if they were a geologic feature, noise, or caused by the instrument. After correlation and with connecting horizons, they now look like fractures. This earthquake shows these fractures the best of all the earthquakes.

The correlation for earthquake 198 isn't as uniformly strong as seen in 191. Looking at the reduced image (Fig. 30), few distinct horizons are immediately identifiable. After correlation, a few horizons have been highlighted in the first multiple. A unique feature of this earthquake is that the second multiple shows more horizons than the first. This indicates more use for multiples than previously expected. The last seismic horizon before the next multiple is also clear and consistent across the seismogram, highlighting the thickness of the layer.

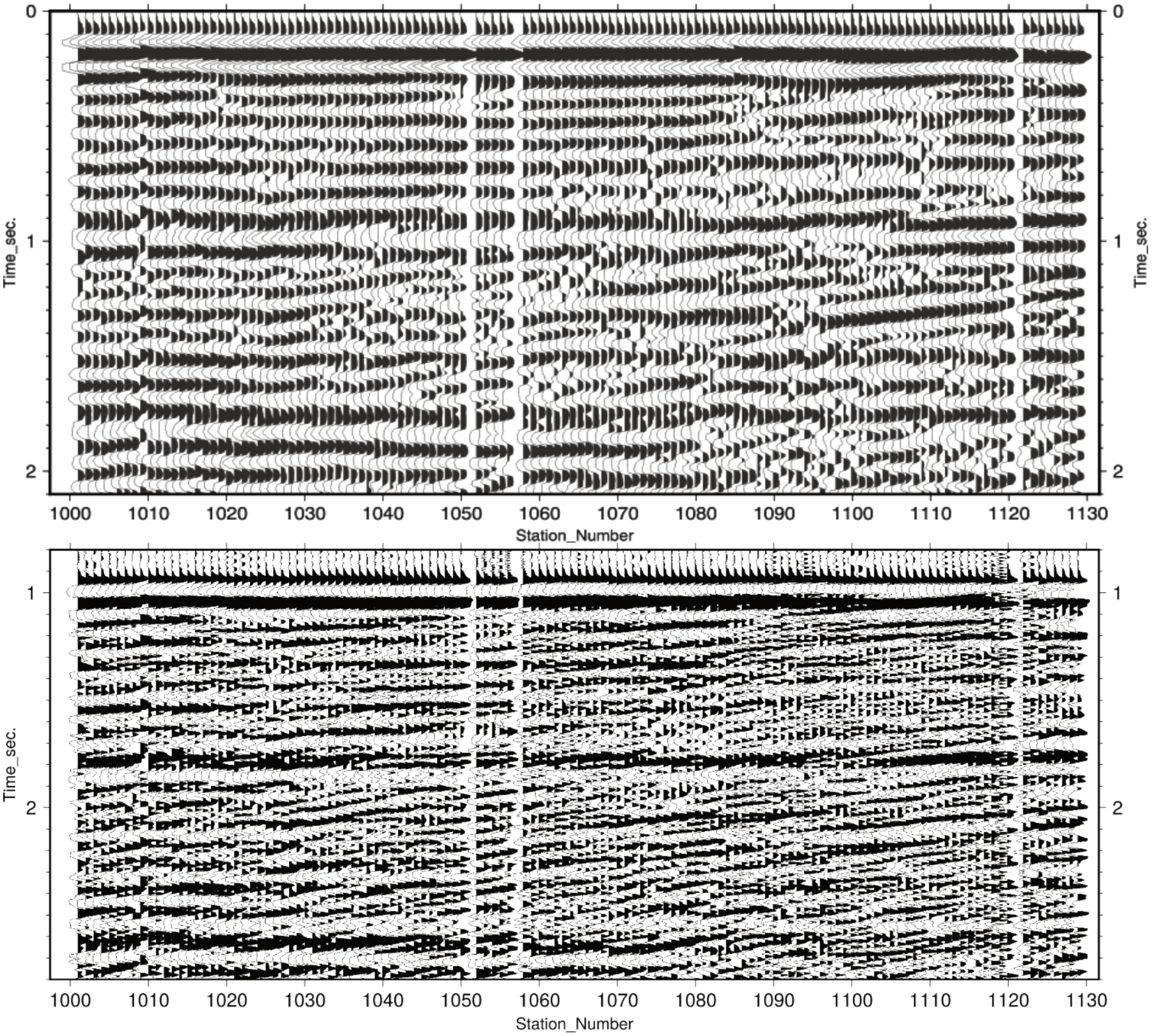

Figure 30: Earthquake 191 comparison of the first 2 multiples of the reduced seismogram (below) and correlated seismogram (above).

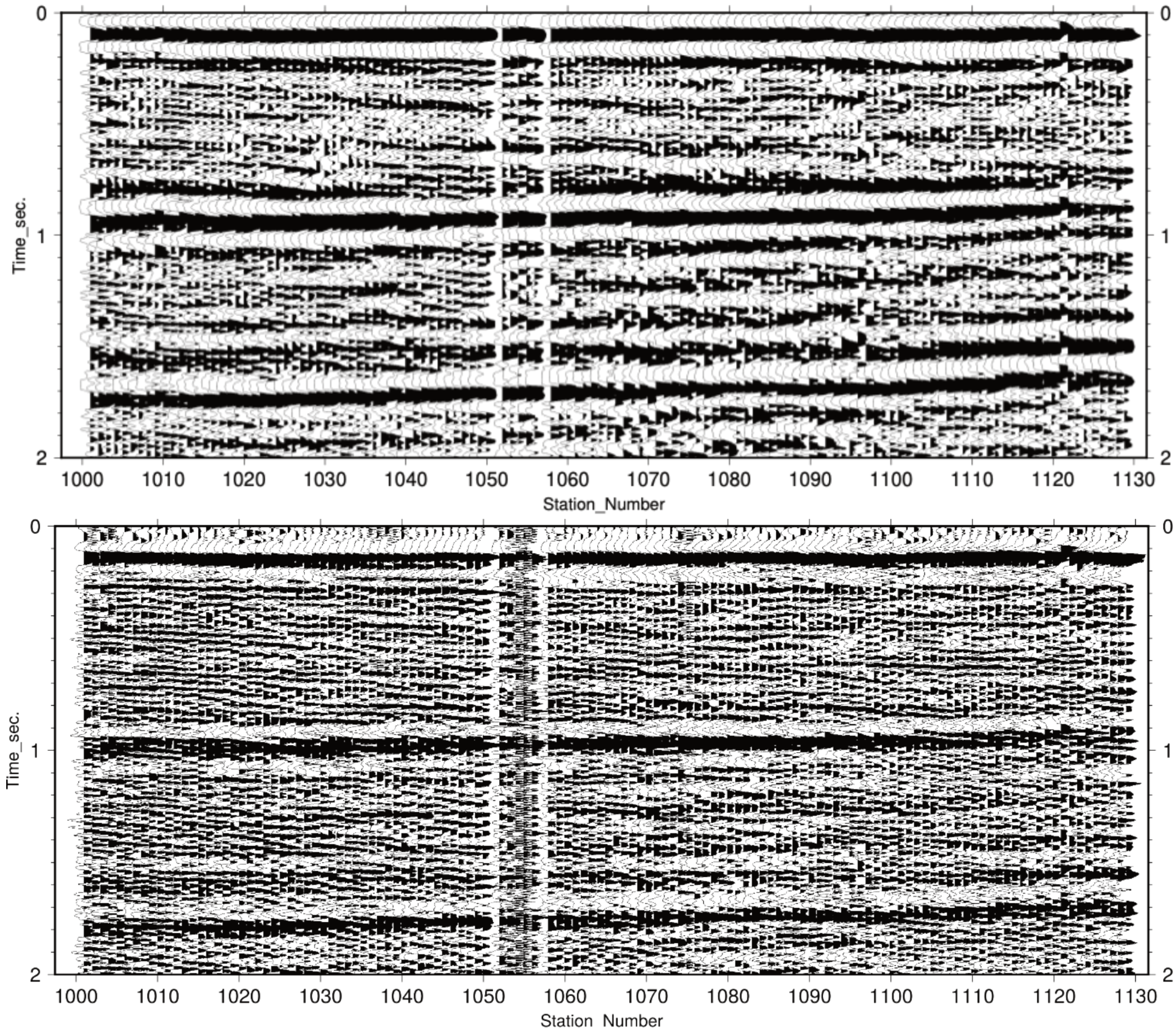

Figure 31: Earthquake 198 comparison of the first 2 multiples of the reduced seismogram (below) and correlated seismogram (above).

Earthquake 197 is the parabolic arrival earthquake. The converging positive peaks of the first arrival are visible in both seismograms (Fig. 31). Unlike the previous earthquakes, this one has weaker horizons to the west. This includes the start of the second multiple that has been strong and consistent before and after correlation. The sloping horizons that are likely fractures discussed in earthquake 191 are visible in the first multiple of the correlated seismogram. Correlating this earthquake did not result in the same array wide improvements seen in the other earthquakes. Several horizons have been strengthened but they do not display the continuity seen previously. Some features were brought out that may otherwise be overlooked. At 0.5s near node 1020 a reflector dips and a short layer begins. A positive peak jump at node 1070 has also been accentuated. Although the correlation does not provide the same utility, it does serve to embolden features that might not be recognized otherwise. The lack of continuous horizons lowers the validity of the seismogram. This is likely a consequence of using a velocity reduction. Similar to the effects of the reduction on a parabolic arrival seen in earthquake 184, data distortion could be the consequence. The original data being parabolic on both sides would encourage more distortion after correlation. Using this reasoning, the most accurate segment of this seismogram would be between nodes 1070 and 1095 where the seismic wave arrived first and before they began their parabolic trend of arrivals. A potential solution to this would be a similar processing method suggested for earthquake 184 to extract more information from the second multiple.

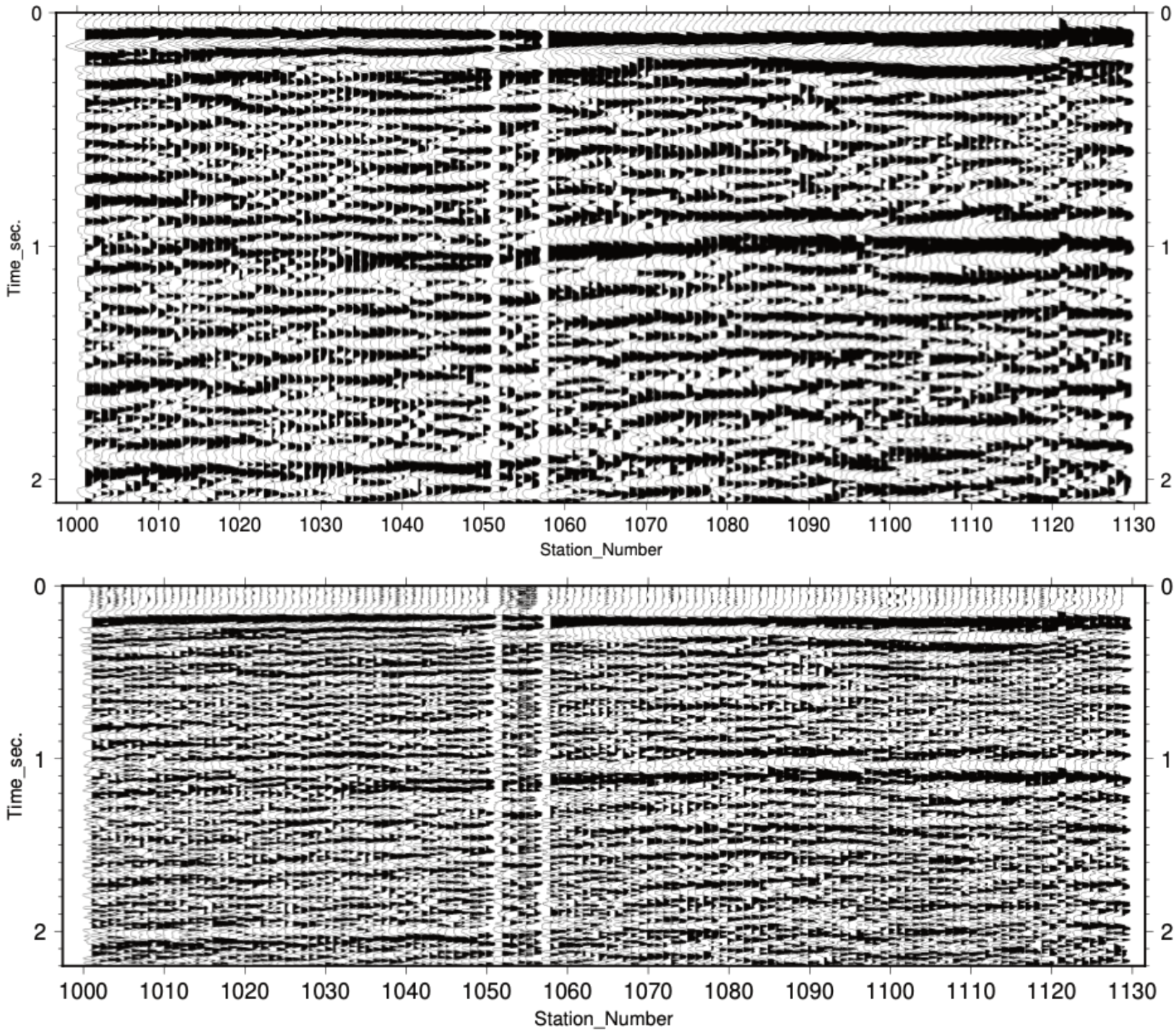

Figure 32: Earthquake 197 comparison of the first 2 multiples of the reduced seismogram (below) and correlated seismogram (above).

Geologic Setting and Well Logs

The Anadarko Basin in a sedimentary basin with a Precambrian igneous basement and mostly sedimentary stratigraphy aged from the Ordovician through Permian. The area of interest (Fig. 33) is on the shelf where deposition either did not occur or the deposits were eroded away for some time periods. For this area the stratigraphy is largely flat and has a negligible dip on the local scale. This region is a large oil and gas producer and has several significant sedimentary packages to identify: the Arbuckle, Simpson, Woodford, Mississippian limestone, and Wolfcampian. The resolution of the seismograms may not be high enough to identify the thin layer.

Using information from isopach maps (Crain and Chang, 2018, 2019) and depths to tops in the area, a stratigraphic column can be constructed to illustrate what to expect. Additional information from the USGS (1995), Davis (1988), and Mitchell (2012) corroborate the information given and summarized in Table 3. Also located 3.13 km south of the array the Trent 1-35SWD well at 36.594258N, 97.797345W (Oklahoma Corporate Commission, 2019). Using the velocity and density logs (Fig. 34) that have been resampled from every 6 inches to every 25 feet, an estimation of the tops and their seismic responses can be made. Please note that the cross section (Fig. 33) is in meters, and the well logs (Fig. 34) and stratigraphic column (Table 3) are in feet.

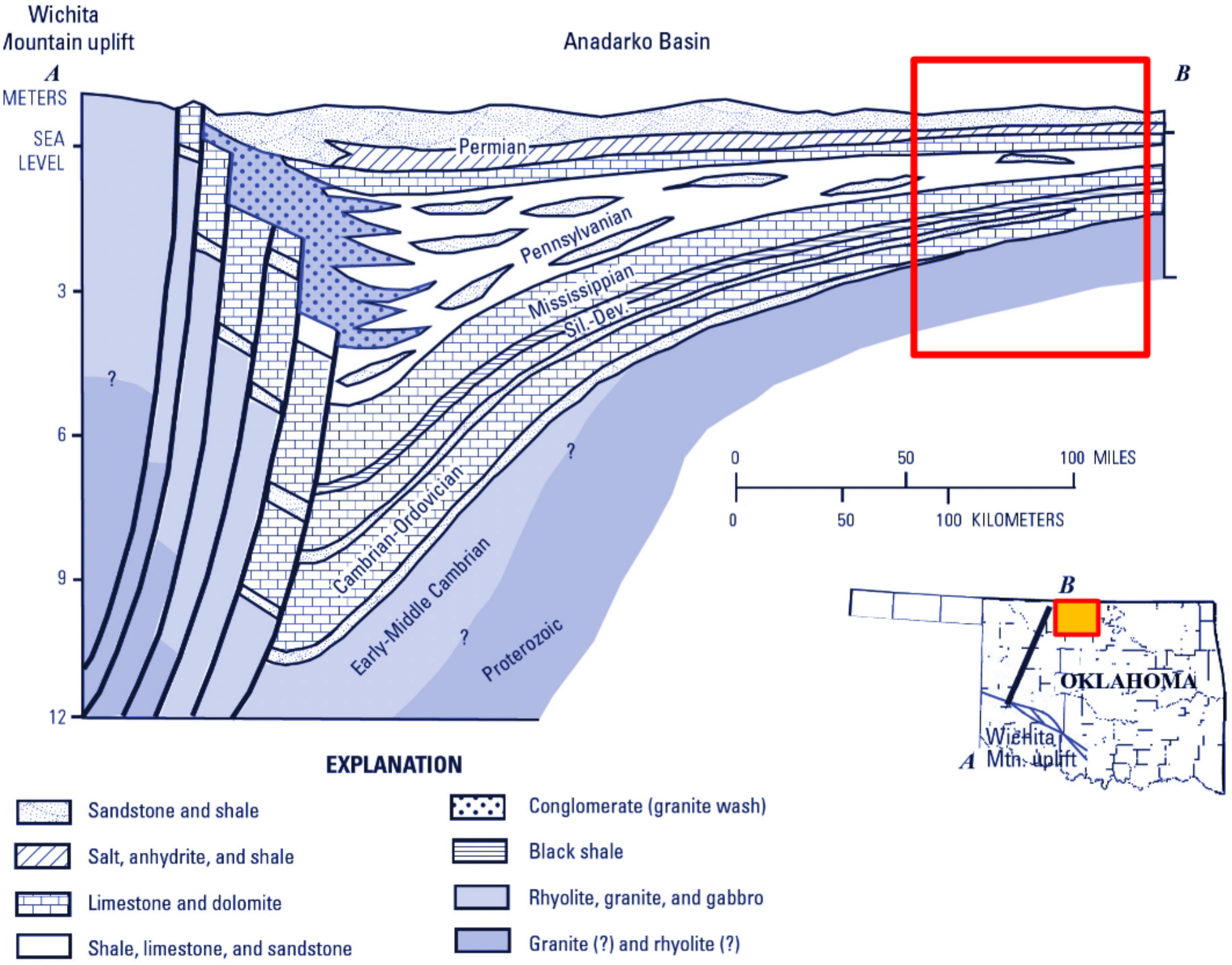

Figure 33: Generalized cross section of the Anadarko Basin modified from Higley, 2014. The slope of the basin shelf has been exaggerated due to scaling. Note that the cross section ends at B, west of the study area. The study area is shown as a red box over the cross section and as an orange box on the inset map for an approximate location in the state.

Table 3: A summarization of the stratigraphic layers of the Anadarko basin in the study area. Depths are approximations based on isopach maps and depth to top reports from the Oklahoma Geological Survey and supported by other works. The depths were taken at ~36.4N, 97.4W on the maps.

Age	**Unit / Series**	**Top depth (feet)**	**Thickness (feet)**
Permian	Leonadrian	Surface	500
Permian	Wolfcampian	500	750
Pennsylvanian	Missourian /Virgilian	1250	1750
Pennsynvanian	Atokan / Desmoinian	3000	1000
Mississippian	Pre-Chesterian Limestone	4000	250
Devonian	Woodford	4250	<100
Ordovician	Viola Limestone	4300	<100
Ordovician	Simpson	4400	300
Ordovician	Arbuckle	4700	1300+
Cambrian	Reagan Sandstone	varies	varies
Pre-Cambrian	Basement	6000 or deeper	

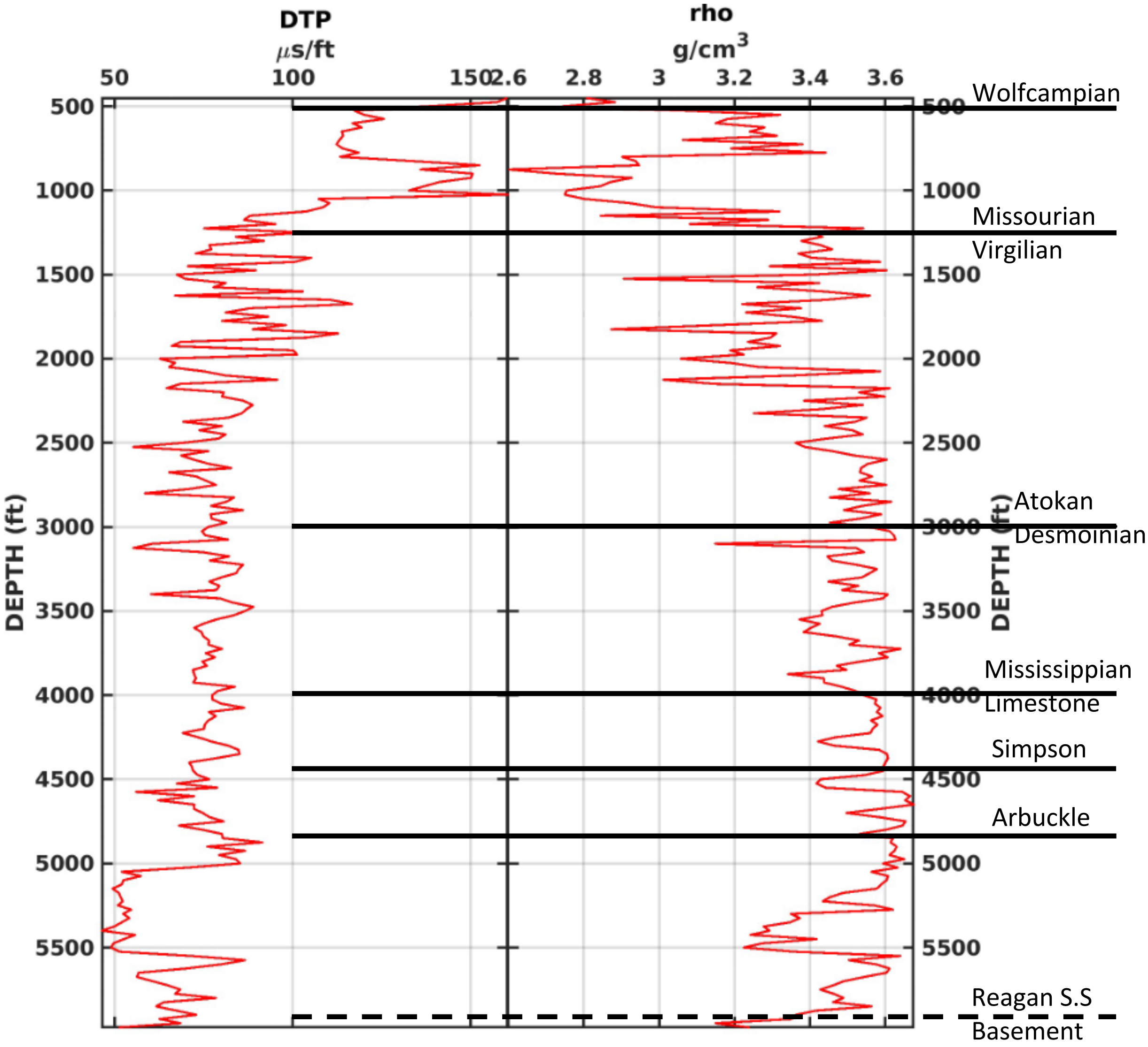

Figure 34: Sonic and density logs from the Trent 1-35SWD well (Oklahoma Corporation Commission, 2019) located 3.13km south of the array. These logs start at ~500 ft and end at ~5900 feet, near where the Arbuckle is expected to end, and have been resampled to every 25 feet. Black lines indicate estimated depths where stratigraphic unit top can be found. The dashed line indicated where the Reagan sandstone, which may not be present in the area, and basement are expected to begin.

Geologic Interpretation

When evaluating the stratigraphic boundaries, the earthquake – array geometries make a difference in where the layers can be identified. As seen in earthquakes 184 and 197 where the arrivals are parabolic and the velocity reduction did not fully raise the seismogram in addition to some layers being squeezed out by faster arrivals, a selection in one seismogram may not fit the other. Other layers may also not be visible at all. The Woodford shale is expected to have a high reflectivity coefficient but it may not be visible due to the resolution of the data and its thin profile at less than 100 ft.

Each earthquake has an interpretation. Permian layers are at the top and usually include the first positive and negative peaks for the Leonardian and Wolfcampian. The Missourian series should be a thicker package followed shortly after, then the Atokan then the Mississippian limestone, a strong (positive or negative) reflector. The Simpson was only identified in earthquake 198 (Fig. 38). The Arbuckle was identified in every earthquake. However, distinguishing between the Arbuckle and basement was difficult in earthquake 191 (Fig. 36). Because earthquakes 184 (Fig. 35) and 197 (Fig. 37) had parabolic arrivals with inconsistent arrival times that were amplified by the velocity reduction, confidently identifying arrivals past the first multiple was not possible.

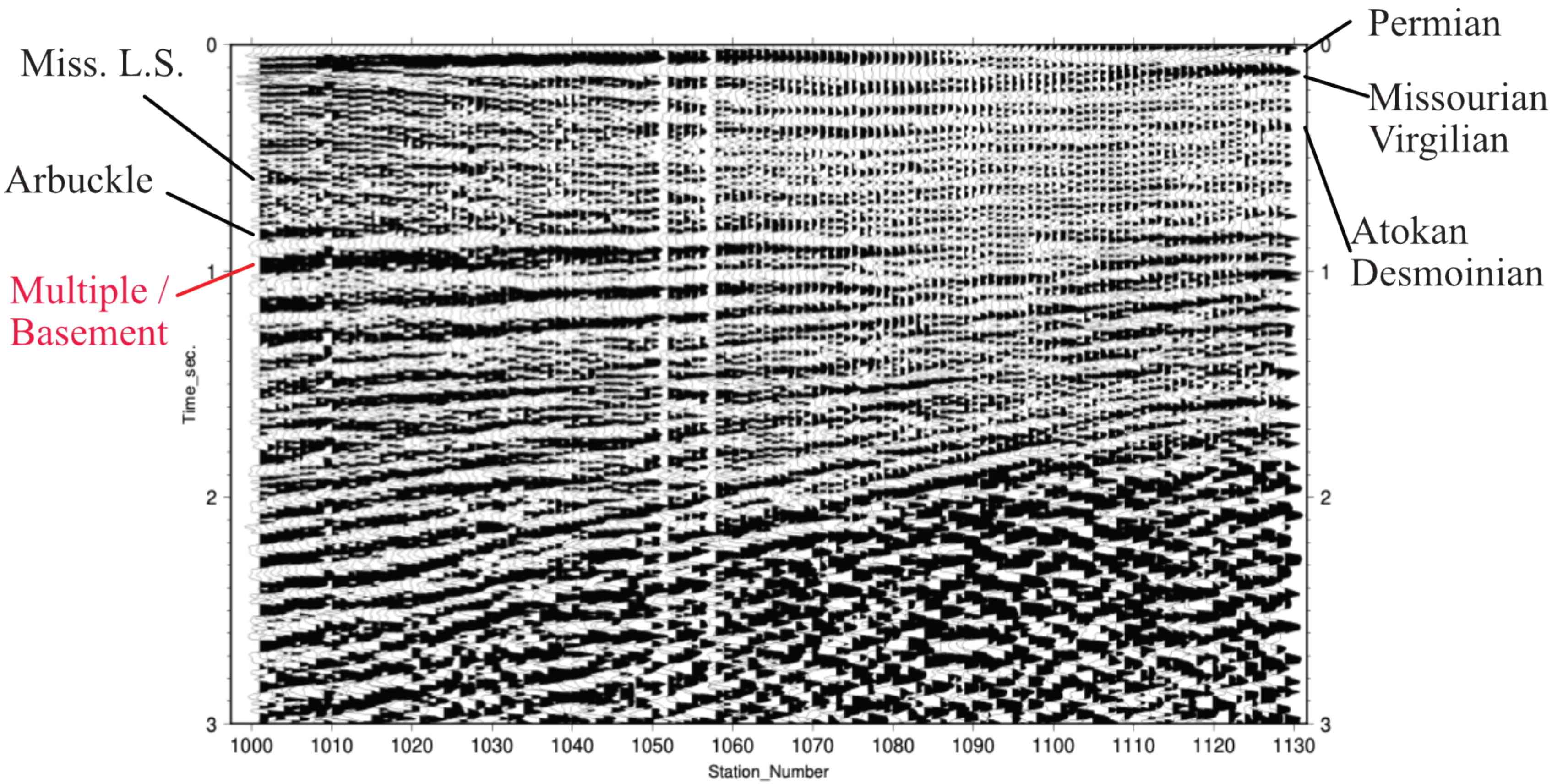

Figure 35: The geologic interpretation of earthquake 184. Because of the poor effects of the velocity reduction, any layers past the first multiple are difficult to identify with confidence. Differentiating between the Permian Leonardian and Wolfcampian is difficult because of the polarity switch. However, the correlation is a displace of similarity, not a true reflection of the subsurface.

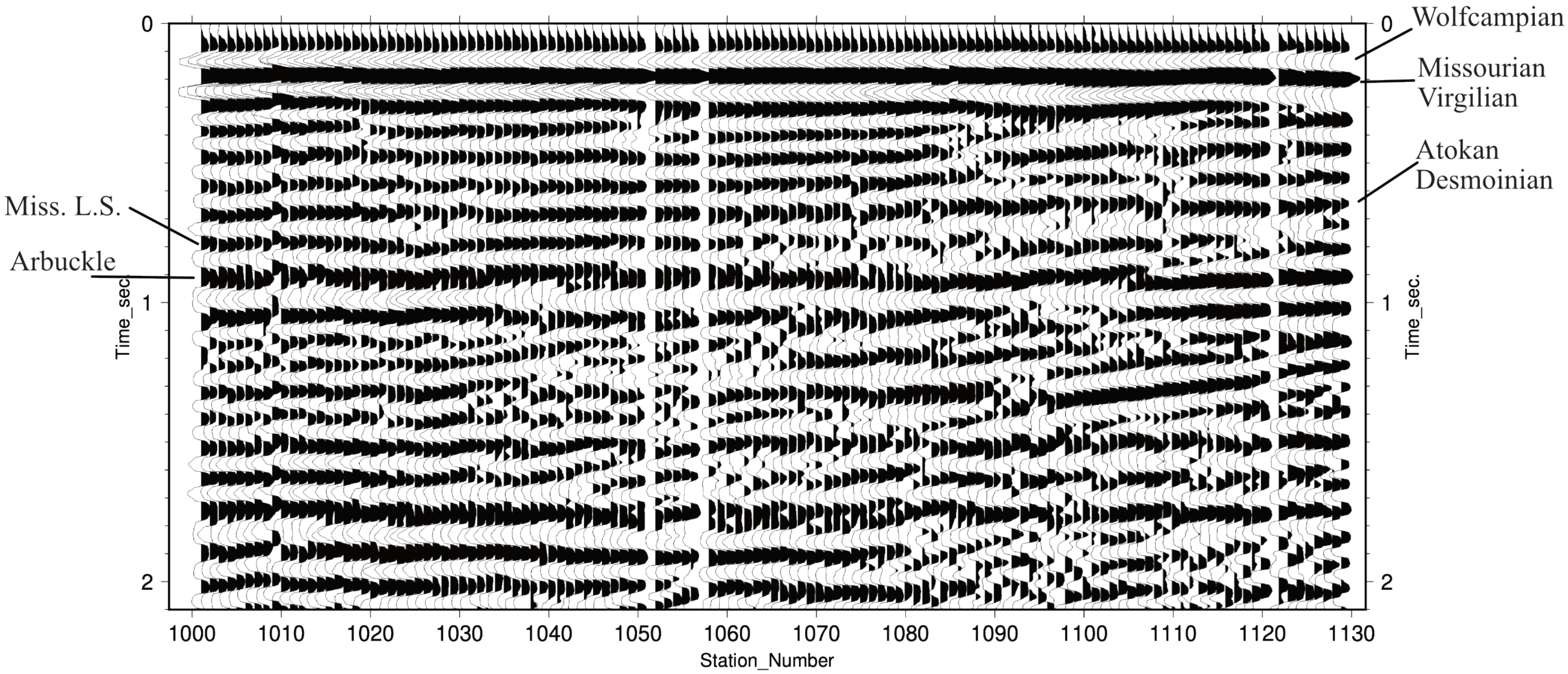

Figure 36: The geologic interpretation of the earthquake 191 correlated image. The regularly spaced horizons of mostly equal amplitude make distinguishing layers difficult. Identification was mostly done based on anticipated layer thickness such as the Missourian / Virgilian. Fractures or faults are visible on the western end of the array

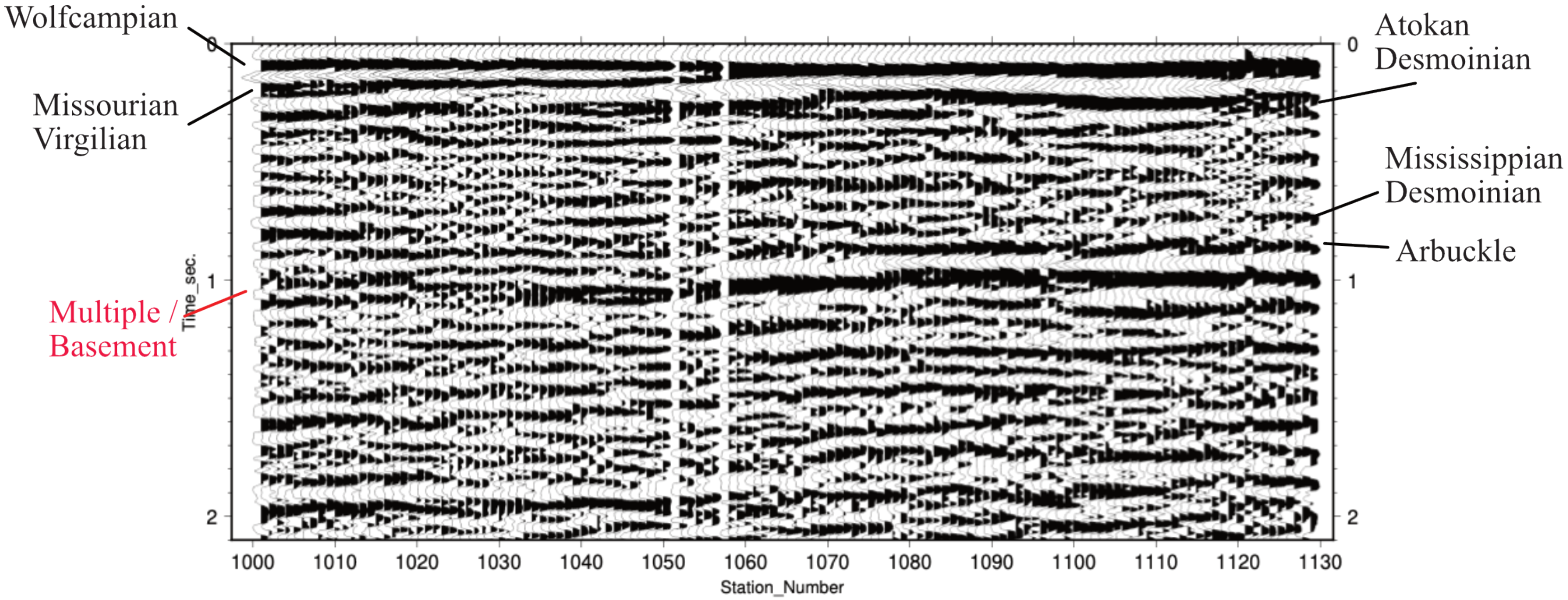

Figure 37: The geologic interpretation of the correlated seismogram of earthquake 197. The horizon splitting leads to different interpretations. The Missourian Virgilian series is a thicker sedimentary package and with two overall densities at ~2100 ft. Following the horizons from either end may leads to two different interpretations. The arrival times and geometry differences across the array obfuscate the continuation of horizons across the array.

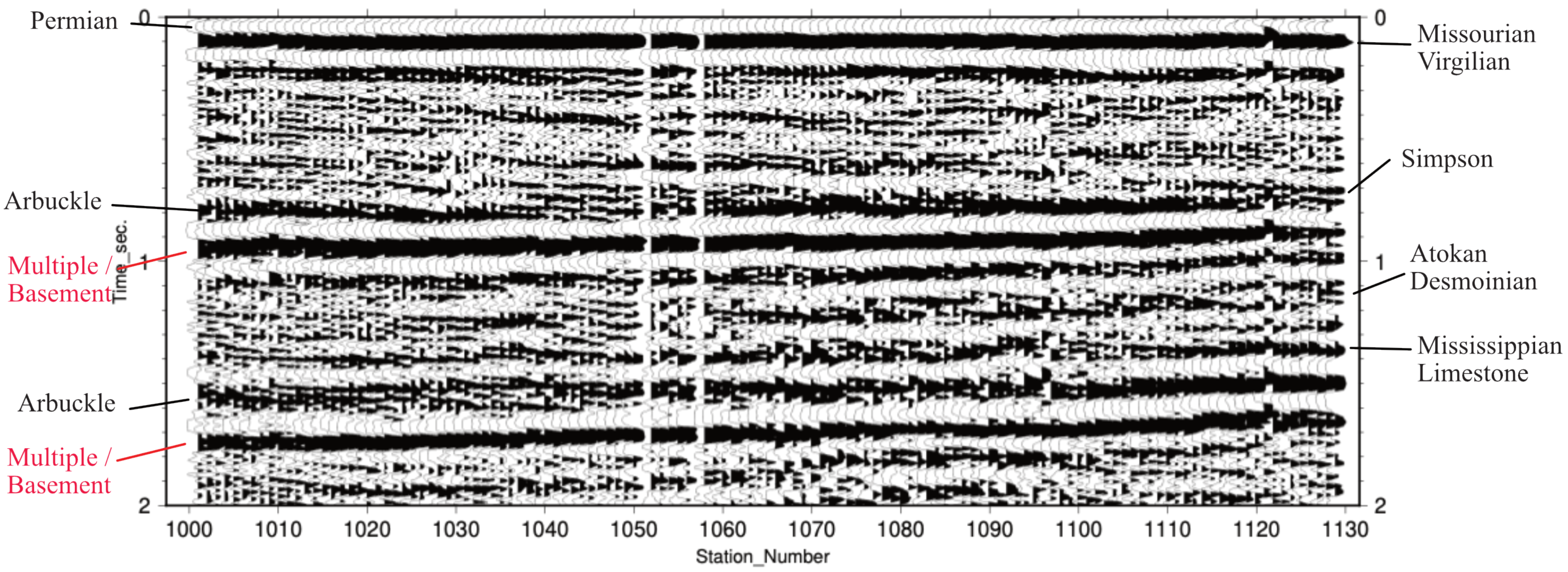

Figure 38: The geologic interpretation of the correlated seismogram of earthquake 198. This seismogram is unique compared to the others in that the second multiple has some interpreted layers. Tracing horizons across the array is not difficult in either multiple but the second has stronger amplitudes in places the first multiple does not. This is the only interpretation with the Simpson series identified above the Arbuckle.

Conclusions and Further Application

A partial autocorrelation is called this because it runs the first arrival wavelet over the original trace instead of the whole trace over itself using the cross-correlation function in Seismic Unix that brings in a separate trace file. It also differs from a cross correlation that typically uses a single trace to pass over each trace from the array instead of the same trace.

Partial autocorrelation has potential to be a strong processing tool. It is a lightweight process that can be done quickly using free software. Results shown in the previous section emphasize its effectiveness at reducing noise and effectively highlighting layer boundaries. An unexpected benefit is how the correlation affects the second, and possibly later, multiples.

Caveats to using the process quickly and "on the fly" are finding the correct reduction velocity. General geologic knowledge of the area can help narrow down the velocity needed for best results but distance from source to receiver and specific geologic characteristic can alter the required velocity. Earthquakes 184 and 197 show the limitations of the process as is. Non-linear seismic arrivals will require different preprocessing for the process to be as effective to those as when applied to linear arrivals. Muting curves may be the solution to this but proved to be no more effective when used on these sample earthquakes.

Torii's theory partial autocorrelation is based on virtually relocates the source, effectively creating a new midpoint. The processed seismograms can be used as a cross section offset from the array. Relocating several cross sections from sources around the around the array can be used to generate a pseudo 3D cross section. Resolving the different resolutions of the correlated seismograms will be key to generating meaningful 3D models with this method. The quality considerations of this method could be offset by its low cost and used as an exploratory method.

REFERENCES

Al-Shaieb, Z., 1991, Compartmentation, fluid pressure important in Anadarko exploration: Oil and Gas Journal, **88**(27), 52–55.

Anderson, K., J. Sweet, and R. Woodward, 2016, IRIS Community Wavefield Experiment in Oklahoma, http://www.fdsn.org/networks/detail/YW_2016/, accessed 18 March 2017, doi:10.7914/SN/YW_2016.

Bakulin, A. and Calvert, R., 2006, The virtual source method: theory and case study: Geophysics, **71** (4), doi: 10.1190/1.2216190

Ball, M. M., M. E. Henry, and S. E. Frezon, 1991, Petroleum Geology of the Anadarko basin Region, Province (115), Kansas, Oklahoma, Texas: U.S. Geological Survey, Open-File Report: 88-450W.

Chopra, S., Marfurt, K., Kolawole, F., Carpenter, B. M., 2018, Nemaha Strike-Slip Fault Expression on 3-D Seismic Data in SCOOP Trend: AASPI publications

Claerbout, J. F., 1968, Synthesis of a layered medium from its acoustic transmission response: Geophysics, **33** (2), 264-269, doi: 10.1190/1.1439927.

Crain, K. D., and Chang, J. C., 2018, Elevation Map of Top of the Crystalline Basement in Oklahoma and Surrounding States: Oklahoma Geological Survey Open-File Report 1-2018.

Dana, G. F., 1955, The subsurface geology of Grant County, Oklahoma, Oklahoma City Geological Society: The Shale Shakers Digest I, 1-5, 298-314.

Davis, H. G., and R. A. Northcutt., 1989, The greater Anadarko basin: an overview of petroleum exploration and development: Anadarko basin symposium, Geological Survey Circular, **90**, 13-24, http://www.ogs.ou.edu/pubsscanned/Circulars/Circular90.pdf.

Draganov, D., Campman, X., Thorbecke, J., and Verdel, A., 2013, Seismic exploration-scale velocities and structure from ambient noise (> 1 Hz): Journal of Geophysical Research: Solid Earth, **118**, 4345-4360, doi:10.1002/jgrb.50339.

Draganov, D., K. Wapenaar, and J. Thorbecke, 2006, Seismic interferometry: Recording the earth's reflection response: Geophysics, **71**(4), SI61-SI70, doi: 10.1190/1.2209947.

Evans, J. L., 1979, Major structural and stratigraphic features of the Anadarko basin *in* Hyne, M. J., Tulsa Geological Society: Pennsylvanian Sandstones of the mid-Continent, 97-113.

Galloway, W. E, M. S. Yancey, and A. P. Whipple, 1977, Seismic stratigraphic model of depositional platform margin, eastern Anadarko basin, Oklahoma: The American Associate of Petroleum Geologists Bulletin, **61**(9), 1437-1447.

Haskel, N. A., 1953, The dispersion of surface waves on multi layered media: Bulletin of the Seismological Society of American, **43**, 17-34.

Havskov, J., and A. Gerardo, 2004, Instrumentation in earthquake seismology: Springer

Henry, M. E., and T. C. Hester, 1995, Anadarko basin province (058), *in* D. L. Gautier, G. L. Dolton, K. I. Takahashi, and K. L. Varnes, eds, National assessment of United States oil and gas resources – results, methodology, and supporting data: U.S. Geological Survey Digital Data series DDS-30, **2**, one CD-ROM.

Higley, D. K., compiler, 2014, Petroleum systems and assessment of undiscovered oil and gas in the Anadarko basin province, Colorado, Kansas, Oklahoma, and Texas—USGS Province 58: U.S. Geological Survey Digital Data Series DDS–69–EE, doi:10.3133/ds69EE

Holloway, S., A. Holland, and G. R. Keller, 2016, Industry contributed fault map of Oklahoma: Oklahoma Geological Society, Open-File Report 2016-1.

Johnson, K. S., 1989, Geologic evolution of the Anadarko basin: Oklahoma Geological Survey Circular, **90**, 3-12

Jorgensen, D. G., 1989, Paleohydrology of the Anadarko basin, central United States: Oklahoma Geological Survey Circular, **90**, 176-193

Keranen, K. M., H. M. Savage, G. A. Abers, and E. S. Cochran, 2013, Potentially induced earthquakes in Oklahoma, USA: Links between wastewater injection and the 2011 M-w 5.7 earthquake sequence: Geology, **41**(6), 699-701, doi: 10.1130/G34045.1

Krzywosz, N., 2015, Investigation of ambient seismic noise using seismic interferometry in western Montana: M.S. Thesis, Montana Tech.

Kunetz, G., and I. d'Erceville, 1962, Sur certaines proproetes d'une onde acoustique plane de compression dans un milieu stratifie: Annales de Geophysique, **18**, 351-9.

Lindzey, K., 2015, Geologically constrained seismic characterization and 3-D reservoir modeling of Mississippian reservoirs, north-central Anadarko shelf, Oklahoma: M.S. Thesis, University of Oklahoma.

Luza, K. V., and J. E. Lawson, 1983, Seismicity and tectonic relationships of the Nemaha uplift in Oklahoma, Part V final report, Oklahoma Geological Survey, Open-file Report OF 1-83

Marsh, S. and Holland, A., 2016, Comprehensive Fault Database and Interpretive Fault Map of Oklahoma: Oklahoma Geological Survey Open-File Report 2-2016.

Mitchell, J., 2012, Anadarko basin: oil and gas exploration – past, present, and future: Oklahoma Geological Survey, https://digitalprairie.ok.gov/digital/collection/stgovpub/id/70300, accessed on 21 April 2018

Mosher, S. G. and P. Audet, 2018, Recovery of P waves from ambient noise interferometry of borehole seismic data around the San Andreas Fault in Central California: Bulletin of Seismological Society of America, **108**(1), 51-65, doi: 10.1785/0120160375

Office of the Secretary of Energy and Environment, 2017, Earthquakes in Oklahoma earthquake map, http://earthquakes.ok.gov/what-we-know/earthquakes-map, accessed on 11 May 2017.

Oklahoma Corporation Commission, 2019, Oklahoma Corporation Commission Imaging – Well Logs, http://imaging.occeweb.com/imaging/OGWellLog.aspx, access on 21 March 2019

Oklahoma Corporation Commission, 2019, Oklahoma Corporation Commission's well data system, http://www.occpermit.com/WellBrowse/Home.aspx, accessed on 5 April 2019

Oklahoma Geological Survey, 2017, 2016 Earthquake catalog accessed on 24 January 2017 at http://wichita.ogs.ou.edu/eq/catalog/2016.

Rietsch, E., 2022, SeisLab 3.02, MATLAB Central File Exchange, https://www.mathworks.com/matlabcentral/fileexchange/53109-seislab-3-02.

Ringler, A. T., R. E. Anthony, M. S. Karplus, A. A. Holland, and D. C. Wilson, 2018, Laboratory Tests of Three Z-Land Fairfield Nodal 5-Hz, three-component sensors: Seismological Research Letters, **89**(5), doi: 10.1785/0220170236

Robinson, E. A., and D. Clark, 2006, Basic seismology – Huygen's Principle: The Leading Edge, **25**(10), 1252-1255, doi:10.1190/1.2360614

Rountree, R. L., 1961, Subsurface geology of Rich Valley and southeast Rich Valley oil fields, Grant County, Oklahoma: M.S. Thesis, University of Oklahoma.

Sherwood, J., and A. Trorey, 1965, Minimum phase and related properties of the response of a horizontally stratified absorptive earth to plan acoustic waves: Geophysics, **30**, 191-197.

Skoumal, R. J., Kaven, J. O., Walter, J. I., 2019, Characterizing seismogenic fault structures in Oklahoma using a relocated template-matched catalog, Seismological Research Letters, **90**(4), 1535-1543, doi.org/10.1785/0220190045

Stein, S., and M. Wysession, 2003, An introduction to seismology, earthquakes, and earth structure: Blackwell Publishing Ltd.

Stockwell, J. W., 2019, Sesmic Unix ver. 44_R16, Colorado School of Mines Center for Wave Phenomena Seismic Unix WIKI, https://wiki.seismic-unix.org/start

Sumy, D. F., E. S. Chochran, K. M. Keranen, M. Wei, and G. A. Aber, 2014, Observations of static Coulomb stress triggering of the November 2011 M5.7 Oklahoma earthquake sequence: Journal of Geophysical Research Solid Earth, **19**(3), 1904-1923, doi: 10.1002/2013JB010612

Sweet, J. R., K. R. Anderson, S. Bilek, M. Brudzinski, X. Chen, H. DeShon, C. Hayward, M. Karplus, K. Keranen, C. Langston, F. Lin, M. B. Magnani, and R. L. Woodward, 2018, A community experiment to record the full seismic wavefield in Oklahoma: Seismological Research Letters, **89**(5), doi: 10.1785/0220180079

Torii, K., T. Matsuoka, K. Onishi, K. Shiraishi, T. Aizawa, Y. Yamanaka, Y. Asano, and T. Takeda, 2007, Application of seismic interferometry to natural earthquakes measured by small-scale array: SEG Technical Program Expanded Abstracts 2007, 1362-1366, doi: 10.1190/1.2792753.

United States Geological Survey, 2021, National Oil and Gas Anadarko basin Province (058), https://www.sciencebase.gov/catalog/item/60c8c754d34e86b9389dc6f0, accessed on 13 March 2023

Walsh III, F. R., and M. D. Zoback, 2015, Oklahoma's recent earthquakes and saltwater disposal: Science Advances, **1**(5), e1500195, doi:10.1126/sciadv.1500195

Wapenaar, C. P. A., J. Thorbecke, and D. Draganov, 2004, Relations between reflection and transmission responses of 3-D inhomogeneous media: Geophysical Journal International, **156**, 179-194.

Wapenaar, K., 2003, Synthesis of an inhomogeneous medium from its acoustic transmission response: Geophysics, **68**, 1756 – 1759, doi:10.1190/1.1620649.

Wapenaar, C. P. A., J. W. Thorbecke, D. Draganov, and J. T. Fokkema, 2002, Theory of acoustic daylight imaging revisited: 72nd Annual International Meeting, SEG, Expanded Abstracts, 2269-2272, doi: 10.1190/1.1817165.

VITA

Alex Eddy was born in Fort Worth Texas and graduated from Castleberry High School in 2005. After serving in the U.S. Marine Corps graduated from Texas Tech University with a B.S. of Geoscience in 2016. Immediately after being accepted to the Master's program at The University of Texas at El Paso under Dr. Steven Harder he began participating in university and Seismic Source Facility projects in Texas, New Mexico, and Colorado. His relevant work experience began with internship was at Los Alamos National Labs under Dr. Ting Chen as part of the Department of Energy Mickey Leland Energy Fellowship in 2017. In 2018 he worked with the Institute of Makers of Explosives on the Derailed Project. His most recent internship was with Mission Support Test Service at the Nevada National Security Site. There he providing project support, seismic monitoring, and catalogued nuclear test records for research purposes and in compliance with the National Archive and Records Administration mandates. After graduating he plans to continue geophysical related field work while developing his programming and GIS abilities.